King Saud University

Arabian Journal of Chemistry

www.ksu.edu.sa
www.sciencedirect.com

ORIGINAL ARTICLE

Synthesis and characterization of CDs/Al$_2$O$_3$ nanofibers nanocomposite for Pb^{2+} ions adsorption and reuse for latent fingerprint detection

B.G. Fouda-Mbanga, E. Prabakaran, K. Pillay [*]

Department of Chemical Sciences, University of Johannesburg, Johannesburg, South Africa

Abstract This study reports a new approach of preparation of carbon dots coated on aluminum oxide nanofibers (CDs/Al$_2$O$_3$NFs) nanocomposite and reusing the spent adsorbent of lead (Pb^{2+}) ions loaded adsorbent (Pb^{2+}-CDs/Al$_2$O$_3$NFs) nanocomposite for latent fingerprint detection (LFP) after removing Pb^{2+} ions from aqueous solution. CDs/Al$_2$O$_3$NFs nanocomposite was prepared by using CDs and Al$_2$O$_3$NFs with adsorption processes. The prepared nanocomposite was then characterized by using UV–visible spectroscopy (UV–visible), Fourier transforms infrared spectroscopy (FTIR), Fluorescence, X-ray diffraction pattern (XRD), scanning electron microscope (SEM), Transmission electron microscopy (TEM), Energy-dispersive X-ray spectroscopy (EDS), Zeta potential, X-ray photoelectron spectroscopy (XPS). The average size of the CDs was 51.18 nm. The synthesized CDs/Al$_2$O$_3$NFs nanocomposite has proven to be a good adsorbent for Pb^{2+} ions removal from water with optimum pH 6, dosage 0. 2 g/L. The results were best described by the Freundlich Isotherm model. The adsorption capacity of CDs/Al$_2$O$_3$NFs nanocomposite showed the best removal of Pb^{2+} ions with q$_m$ = (177. 83 mg/g), when compared to the previous reports. This adsorption followed the pseudo-second order kinetic model. ΔG and ΔH values indicated spontaneity and the endothermic nature of the adsorption process. CDs/Al$_2$O$_3$NFs nanocomposite therefore showed potential as an effective adsorbent. The data were observed from adsorption–desorption after 6 cycles which showed good adsorption stability and re- usability of CDs/Al$_2$O$_3$NFs nanocomposite. Furthermore, the spent adsorbent of Pb^{2+}-CDs/Al$_2$O$_3$NFs

[*] Corresponding author.
E-mail address: kriveshinip@uj.ac.za (K. Pillay).

ELSEVIER **Production and hosting by Elsevier**

nanocomposite has proven to be sensitive and selective for LFP detection on various porous substrates. Hence Pb^{2+}-CDs/Al$_2$O$_3$NFs nanocomposite can be reused as a good fingerprint labelling agent in LFP detection so as to avoid secondary environmental pollution by disposal of the spent adsorbent.

1. Introduction

Heavy metals are considered as primary pollutants due to their mobility and toxicity in natural water systems. Among the various heavy metals, Lead is considered as an extremely toxic metal as it poses health problems to human beings and the environment at very low concentrations in water (Al Naggar, 2018; Gautam et al., 2016). The major sources of lead contamination in water are from the discharge of wastewater from different industries such as mining, metallurgical processes, electroplating, and plastics manufacturing (Jaishankar et al., 2014). Lead has been found in the water of numerous public housing estates, particularly those opened the in the past decade (Kang-Chung Ng 2015). Additionally, Pb^{2+} and PbO were also used as efficient and selective catalysts for the reduction of target products, which is based on the physical and chemical properties of catalysts. Pb-doped BiFeO$_3$ on reduced graphene oxide (rGO) sheets (Pb-BFO/rGO) was used as a heterogeneous catalyst for the photocatalytic degradation of perfluoroocatanoic acid (PFOA) under the microwave enhanced Fenton method (Li et al., 2017). Pb-CeO$_2$-WO$_3$ and PbO-Mn-Ce/TiO$_2$ catalysts exhibited the best catalytic activity and selective catalytic for the reduction of NO into NH$_3$ (Peng et al., 2016a, 2016b; Zhou et al., 2016). Pb-CeO$_2$ was found to be an active catalyst and it enhanced the photocatalytic reduction of cationic and anionic dyes under visible irradiation at room temperature and atmospheric pressure (Shajahan et al., 2020).

The removal of such heavy metals from aqueous solution has been conducted using various techniques such as chemical precipitation, ion exchange, electroflotation, membrane filtration and reverse osmosis (Gunatilake 2015). All these methods generally have demerits and these include improper adsorption removal, high cost, high energy demands, and they also lead to the generation of toxic sludge which is undesirable. Hence there is a need to develop eco-friendly methods to reduce waste and eliminate heavy metals with lower concentration. The most popular technology used for heavy metal removal is the adsorption method, which is easy, convenient, and has demonstrated increased adsorption removal efficiency (Luisa Cervera et al. 2003; Santos Yabe and de Oliveira, 2003). Hence, mostly low cost adsorbents have been used to increase the adsorption efficiency of lead with less concentration (Zhu et al., 2018; Yang et al., 2019). The low cost adsorbents used included apricot stone activated carbon, peat moss-derived biochar, Gingelly oil cake and cactus (Opuntia ficus indica) cladodes which gave enhanced the adsorption capacities which corresponded to 111.11 mg/g, 81.3 mg/g, 105.26 mg/g, and 98.62 mg/g (Barka et al., 2013; Lee et al., 2015; Nagashanmugam and Srinivasan, 2010).

However, this method depends on the type of adsorbents used (Wang et al. 2019; Zheng et al., 2018). Other adsorbents which have been used include zeolites, clays, activated carbons, carbon materials, metal oxides, and modified nanoparticles (Bee et al., 2011; Guerra et al., 2008; Venkatesan et al., 2014; Zhang et al., 2011). Nanoparticles were explored as adsorbents due to their unique properties such as large surface area, large pore volume, better pore size, easy surface functionalisation and easy modification. Therefore, modified nanomaterials can enhance the removal of metal ions because of electrostatic interactions between the adsorbent and metal ions (Hua et al., 2012; Madrakian et al., 2013a). However, these show low adsorption capacities for metal ions without supporting agents (Mahdavi et al., 2013, Mahdavi et al., 2012). Hence, metal oxides were capped with different capping agents such as walnut shell, 1,5-diphenyl carbazon, CNT/

Al$_2$O$_3$, CNT/MnO$_2$, Polypyrrole-Polyaniline/Fe$_3$O$_4$ and ZnO@Chitosan core/organically shell nanocomposite (ZOCS), which increased the adsorption capacity and resulted in better removal of heavy metal ions (Hsieh and Horng, 2007; Mahdavi et al., 2015; Wang and Ariyanto, 2007). Recently, chitosan and organic materials were modified with magnetic and titanium oxide nanoparticles to improve adsorption capacity (Salam et al., 2011; Madrakian et al., 2013b). There is however a drawback in the preparation of metal oxide nanoparticles due to high cost and high toxicity.

Therefore, there is a growing interest in using low cost and easily available materials for the adsorption of metal ions. Various types of agricultural waste materials like rice husk, sugarcane bagasse, sawdust, brazil nutshell, grape stack, mango peels and coconut copra meal have been used as adsorbents for the removal of lead and other heavy metal ions from wastewater (Mdoe, 2014; Meepho et al. 2018). Recently, it was reported that functional groups such as carboxyl, hydroxyl, phosphate, thiol and amine groups which are present in agricultural waste, biomass play an important role in the binding of heavy metals. These functional groups are bound with the metal through ion exchange by transferring hydrogen ions or through the complex formation by sharing an electron pair (Farooq et al., 2010). Most of these agricultural materials showed superior adsorption capacities when compared to granular activated carbon (Das et al., 2012; Ntuli and Hapazari, 2012).

Carbon dots (CDs) supported metal oxide nanoparticles which were obtained from fruit and vegetable waste materials such as orange peels, banana peels, cabbage waste, and lemon peels have demonstrated advantages such as biocompatibility, non-toxicity, photoluminescence and environmental friendliness (Sagar et al., 2018; Shi et al., 2019; Cruz et al., 2017; Liu et al., 2015). In addition, the different functional groups found in C-dots such as carbon, oxygen, and other heteroatoms vary significantly and can strongly interact with metal oxide nanoparticles (Fernandes et al., 2015).

Banana is a source of vitamin B6, fibers, potassium, magnesium and vitamin C which play an important role in human health such as digestion and weight control (Bertoia et al., 2015; den Besten et al., 2013). Furthermore, banana including the peels is rich in C, O, and H which are mainly found in functional groups such as hydroxyl and carboxylic groups on the surface of carbon dots. These functional groups contribute to improving water solubility and enhancing luminescence (Bourlinos et al., 2015; Xu et al., 2015).

Metal oxide nanoparticles represent a field of materials chemistry which attracts considerable interest due to the potential technological applications of these compounds. The impact of using these materials in fields such as medicine, information technology, catalysis, energy storage and sensing has driven much research in developing synthetic pathways to such nanostructures (Corr, 2012). Today metal oxides are used as labeling agents and have attracted many researchers in the domain of fingerprints. These include metal oxides such as SiO$_2$, SnO$_2$, ZnO and CeO$_2$ (Moret et al., 2016; Qin et al., 2013; Peng et al., 2016a, 2016b; Rohini et al., 2017). Among them Al$_2$O$_3$ is one of the most important and extensively used ceramic materials as an adsorbent for water and wastewater treatment, catalysts or catalyst supports for chemical reactions, electrical insulators, structural composites for spacecraft, abrasive, thermal wear coatings and membrane applications (Sharma et al., 2010; Srivastava et al., 2011; Yalamaç et al., 2014; Cai et al., 2015). Al$_2$O$_3$ nanoparticles are cost-effective nanomaterials possessing high surface area as well as mechanical strength, and they have exceptional chemical stability towards high

temperatures and harsh conditions such as the abrasive environment. Furthermore, they possess low electrical conductivity (Bala et al., 2011; Mukherjee et al., 2011).

After these nanomaterials are used as adsorbents they are either discarded in the environment leading to secondary pollution or regenerated for use (Zwain et al., 2014). Once the metal is recovered from the adsorbent's surface, the problem of how to get rid of the spent adsorbent needs to be considered. The metal ion attached on the adsorbent also creates disposal problems as it is a hazardous material. This approach leads to the problem of huge deposits of spent adsorbents within a short period of time and the financial cost in pre-treating the solid waste before disposal (Omorogie et al., 2016). To date little work has been conducted on the reuse of these spent adsorbents after they have been applied in the removal of the desired pollutants. Hence, this means the development of a method to reuse the adsorbed metal is still a challenge. Developing a reuse application for the heavy metal loaded adsorbent is crucial since this will avoid secondary pollution. Such metal-loaded adsorbents can be reused as cement additives and anti-bacterial applications.

Additionally, it could also be useful in real life issues such as crime scene investigations, in which latent fingerprint detection (LFP) is an essential tool which is used to provide evidence against criminals in a court of law (Basavaraj et al., 2017; Li et al., 2016a, 2016b). The fingerprint image shows different features such as ridge and furrow patterns. Two fingerprint images do not show similar features at crime scenes and are classified into three types namely patent, plastic and latent fingerprints. Fingerprint patterns are obtained from different substrates on contact with paint, ink and blood to obtain clear fingerprint images. Plastic fingerprints have been observed on smooth surfaces such as clay, wax and wet paint. LFP images do not readily show the image and ridge detail and this requires chemical processes. The physical evidence of LFP detection depends on the use of fingerprint powder materials to produce variation between the sweat of the fingerprint and substrate (Niu et al., 2015). In this sense, nanoparticle powders have the advantage of high surface area, good luminescence, reduced background, nontoxicity, good stability, eco-friendliness and also electrostatic forces between the positive charges of fingerprint sweat and negative charges of nanoparticles for the development of LFP (Chen et al., 2016; Cantu, 2001).

For instance Aluminum oxide based nanoparticles were also used for the investigation of LFP detection because these are good labeling agents and minimize the background interference. Modifiers such as natural dyes, organic groups and metal ions on aluminum oxide nanoparticles were reported to improve LFP detection. Such materials also present the advantages of less background interference, high visibility and better adherence to oily compounds of fingerprint residue with different substrates (Kim et al., 2016; Das and Shama, 2016). Different common powders and some fluorescent powders were used to develop fingerprint images with ridge details (Song et al., 2012). The powder dusting method was found to be a suitable and better method for improving latent fingerprint detection (Champod et al., 2016). The LFP residue contains different compounds such as sweat, amino acids, proteins, lipids, creatinine, choline, and lactic acid (Sodhi and Kaur, 2016). The selection of the powder dusting method is an important aspect of the development of fingerprint images and viewing ridges under daylight conditions in the sense that the powder is also easily bound with organic compounds.

To our best knowledge, there are no literature reports on the reuse application of latent fingerprint detection after adsorption of lead or other metal ions on adsorbents. This present work therefore aimed at preparing carbon dots supported on an aluminum oxide nanofibers nanocomposite for the removal of lead ions from aqueous solution and explored the reuse of the lead ions loaded adsorbent for latent fingerprint detection. The carbon dots were synthesized from banana peel waste using a hydrothermal method. Al_2O_3NFs were prepared from aluminum isopropoxide by a sol–gel method. CDs/Al_2O_3NFs nanocomposite was prepared by the adsorption method. Then CDs/Al_2O_3NFs nanocomposite was used for lead ion removal with batch experiments setup and also optimized of various process parameters like initial pH, contact time, adsorbent dose and initial metal ion concentration. Then, lead ion loaded on Pb^{2+}-CDs/Al_2O_3NFs nanocomposite adsorbent was used for latent fingerprint detection by the powder dusting method.

2. Materials and methods

2.1. Materials

Banana peels waste from bananas, which were purchased from a retail market in Johannesburg, South Africa, was used to prepare the carbon dots. Aluminum isopropoxide (C_9H_{21}-AlO_3), Cadmium(II)nitrate tetrahydrate ($Cd(NO_3)_2 \cdot 4H_2O > 98\%$), Nickel(II) nitrate hexahydrate ($Ni(NO_3)_2 \cdot 6H_2O > 98\%$), Copper(II)nitrate trihydrate ($Cu(NO_3)_2 \cdot 3H_2O > 99–104\%$) and Manganese(II) chloride tetrahydrate ($MnCl_2 \cdot 6H_2O > 98\%$) from Sigma Aldrich (South Africa). Lead(II) nitrate ($Pb(NO_3)_2 > 99\%$) purchased from Merck (South Africa), KBr, NaOH (>99.9% grade), HCl, Ethanol and Dialysis cellulose membranes 12,000 MW were purchased from from Merck (South Africa). Ultrapure de-ionized water (resistivity > 18.5MX cm) was used to prepare the working solutions and was obtained from water purification systems (Milli-Q, Millipore). Solvents and other chemical compounds have been purchased from Sigma-Aldrich and were of reagent grade.

### 2.2. Preparation of CDs by hydrothermal method

The banana peels from bananas purchased from a retail marked in Johannesburg, South Africa were washed with water several times to remove ash and other contaminants. After some time, the banana peels were washed with distilled water until the dust was removed. The washed banana peels were cut into pieces and transferred into a beaker which was then dried in an oven at 80 °C for 12 h. The dried peels were ground and stored in 50 mL plastic vials. Carbon dots were synthesized using 2.0 g of banana peels which was mixed with 50 mL of deionized water and stirred for 30 min to homogenize the mixture. This mixture was then transferred into an auto-clave reactor which underwent hydrothermal treatment at 180 °C for 12 h. The solution obtained after hydrothermal treatment was centrifuged and the supernatant liquid was dialyzed and later freeze-dried as shown in scheme 1.

2.3. Preparation of Al_2O_3NFs by using Sol-gel method

Aluminum oxide nanoparticles were synthesized using 1.02 g of aluminum isopropoxide mixed with 50 mL of ethanol, 10 mL of water and 2.5 mL ammonium hydroxide. The solution was stirred for 24 h and then centrifuged. The collected Al_2O_3 was then calcinated at 550 °C for 5 h. After calcinations, the Al_2O_3NFs were crushed into a fine powder. The synthesis of Al_2O_3NFs is summarized as shown in Scheme 2.

2.4. Preparation of CDs/Al_2O_3NFs nanocomposite by adsorption method

The CDs/Al_2O_3NFs nanocomposite was synthesized using CDs powder (15 mg) and Al_2O_3NFs (100 mg) dissolved into
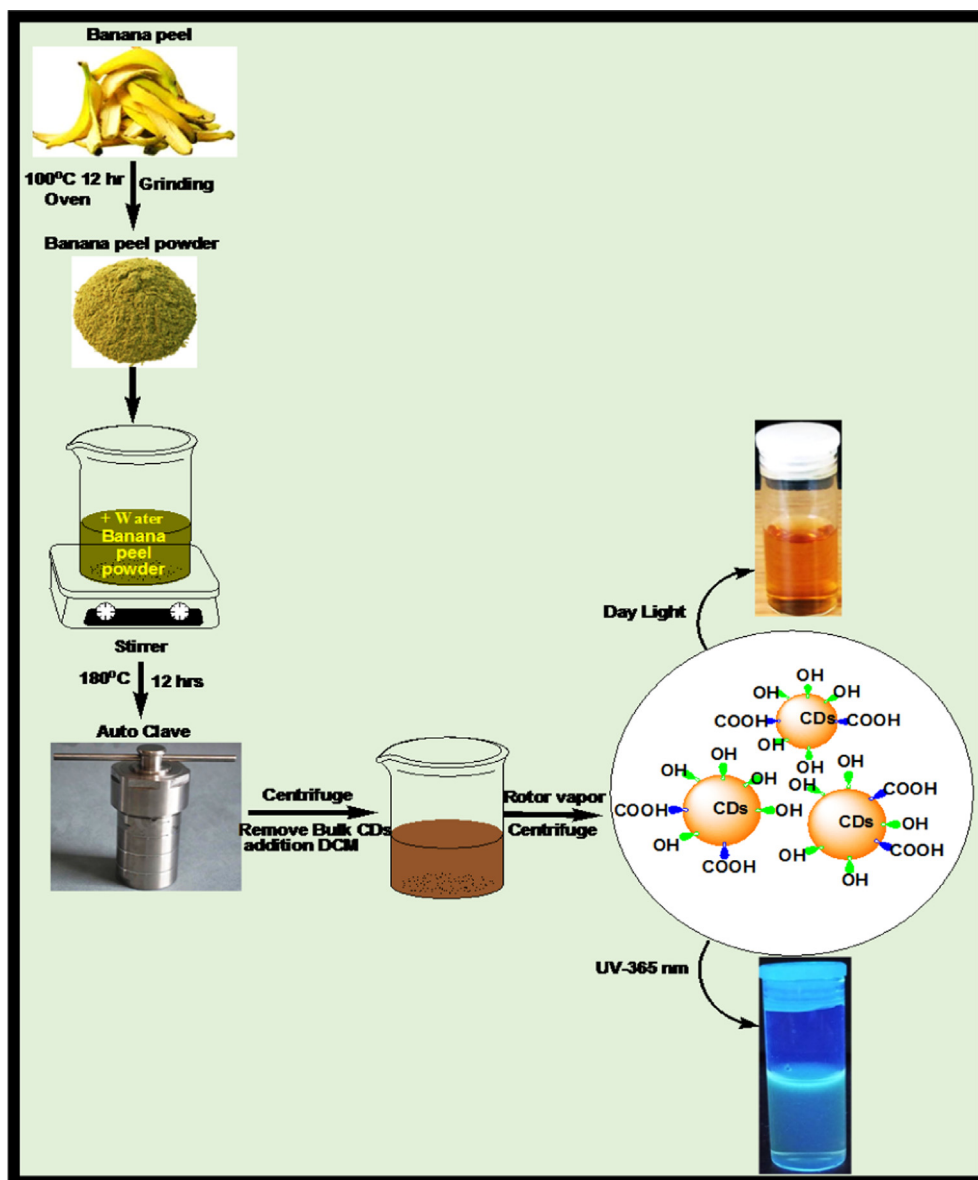
Scheme 1 Schematic diagram of synthesis of CDs from banana peel by hydrothermal method.

20 mL of deionized water (H$_2$O) while stirring at room temperature for 24 h. Then the solution was centrifuged and CDs/Al$_2$O$_3$NFs nanocomposite was collected, dried and crushed into a powder. The preparation processes are shown in Scheme 3.

### 2.5. Characterization techniques

FT-IR spectrum of Carbon-dots, Al$_2$O$_3$ nanofibers and CDs/Al$_2$O$_3$NFs nanocomposites was analyzed by (Perkin Elmer, USA) Bruker Vertex 70 FT-IR Spectrometer (2:100 adsorbent: KBr ratio) within a range of 4000–400 cm^{-1} to identify functional groups. A Remi Orbital Shaker was used for the agitation of the solutions, Shimadzu UV-1208 model UV–visible spectrophotometer (Japan) was used for UV–Visible analysis. The size of CDs, Al$_2$O$_3$NFs and CDs/Al$_2$O$_3$NFs nanocomposite were determined using Transmission Electron Microscopy (TEM) (TEM JEOL, JEM-2100F) with an electron accelerating voltage of 90 kV. The morphology and elemental composition of the nanomaterials were investigated using a Scanning Electron Microscope (Tescan, Vega SEM) at the electron acceleration voltage of 20 kV with carbon coating for image quality. XRD (Panalytical X-PertPro X-ray Diffractometer with Philips PW1729 diffractometer with working systems of Cu Kα radiation (λ = 1.5406 Å) operating at 45 kV and 40 mA)). Raman spectroscopy was used to identify the stretching vibration modes of nanoparticles with an operating system of PerkinElmer Spectrum with two spectrometers at a laser excitation line of 532 nm. A zeta sizer (Malvern) was used to find the stability and charge of the synthesized nanocomposite. Size distribution and zeta potential measurements of the
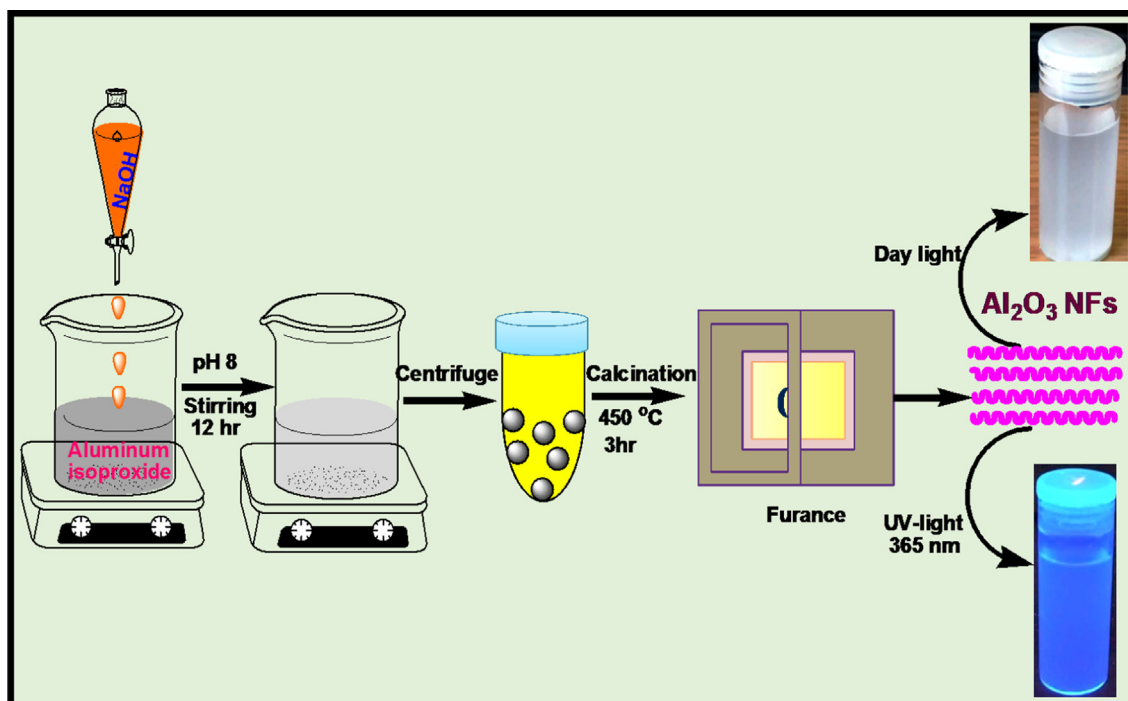
Scheme 2   Schematic diagram of synthesis of Al$_2$O$_3$NFs by using Sol-gel method.
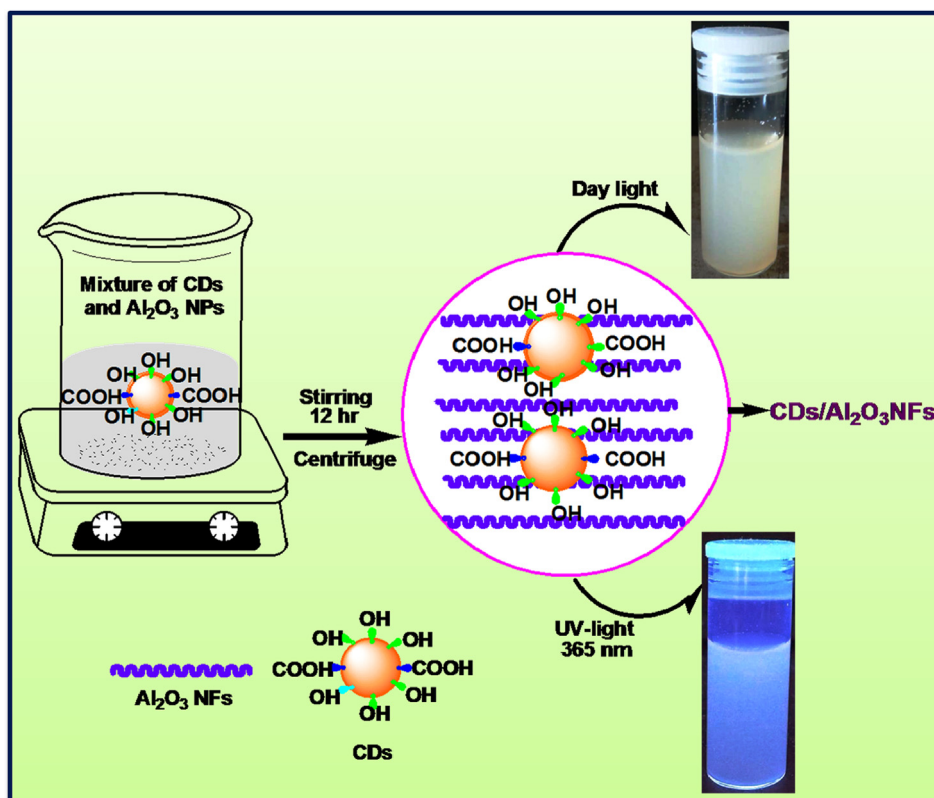
Scheme 3   Schematic diagram of CDs/Al$_2$O$_3$NFs adsorbent by adsorption method.

CDs were conducted using a Malvern Zetasizer Nano ZS 90. Inductively coupled Plasma Optical Emission Spectrometer (ICP-OES) was used to determine the Pb^{2+} ions concentration after adsorption (Shimadzu, Japan) at a wavelength of 221.10 nm at 0.5 mL/min pump speed. Argon gas was used to generate the plasma. The pH measurements were conducted

with an OHAUS Corporation starter 2100 (USA) used to adjust the pH of the solution. The latent Fingerprint images and fluorescence images were captured under normal visible light using a phone camera.

2.6. Batch adsorption studies

Pb^{2+} ions removal test solutions were prepared from the stock solution. Adsorption studies were conducted in triplicate in plastic containers using 20 mL of 20 mg L^{-1} Pb^{2+} ions solution at pH 6.0 ± 0.2 and 0.2 g of adsorbent, followed by shaking in a thermostatic water bath shaker at 200 rpm for 5 h. The pH influence was established by varying the initial pH (1–10) using 20 mg L^{-1} of Pb^{2+} ions solution. The pH adjustment was conducted using 0.1 M HCl and 0.1 M NaOH solution. The amount of lead adsorbed onto CDs/Al₂O₃NFs nanocomposite was calculated by using mathematical mass balance equation as shown in Eqs. (1) and (2).

$$q_e = \frac{(C_o - C_e)V}{m} \tag{1}$$

where qe (mg g^{-1}) and V (L) denote the equilibrium amount of Pb^{2+} ions per unit mass of adsorbent and the solution volume, respectively.

$$\text{Removal efficiency}\,(\%) = \frac{C_0 - C_e}{C_0} \times 100 \tag{2}$$

C_e is the metal concentration in solution at equilibrium; Co is the initial concentration, v is volume of solution in liter and m is the mass of adsorbent in grams.

A comparative study was conducted to comprehend the adsorption accomplishment and adsorption mechanism. To accomplish this, adsorption isotherms were investigated at pH 6.0 ± 0.2 for different temperatures (25 °C, 30 °C, 35 °C and 40 °C) with initial Pb^{2+} ions concentration ranging from 10 to 80 mg L^{-1} and 0.2 g adsorbent dose. The experiment was conducted in triplicate. The isotherm data associated with the adsorption process were used to determine the thermodynamic parameters such as Gibbs free energy (ΔG°), enthalpy (ΔH°) and entropy (ΔS°) change. Adsorption kinetics is essential for the prediction of the rate and modeling of water treatment systems. This was studied using 20 mL solutions of different initial Pb^{2+} ions concentrations (10, 20, 40 and 80 mg L^{-1}) at 25 °C, 0.2 g adsorbent dose and pH 6.0 ± 0.2 for 0 to 300 min shaking. The adsorption capacity of the adsorbent (qt) at time t was obtained using Equation (3):

$$q_t = \frac{(C_o - C_t)}{m} v \tag{3}$$

where qt (mg g^{-1}) and C_t (mg L^{-1}) represents the quantity of Pb^{2+} ions taken up per unit mass of adsorbent and the concentration of Pb^{2+} ions at time t, respectively.

2.7. Effect of competition ions

The effect of competing ions is crucial in adsorption studies because no single ion is found alone in natural water bodies. Therefore it was important to check the influence of other divalent ions on the binding site of CDs/Al₂O₃NFs nanocomposite with above-mentioned method. This was achieved by dissolving precursor salts of the selected ions (Cd^{2+}, Cu^{2+}, Mn^{2+}, Ni^{2+}, Zn^{2+}) together with Pb^{2+} ions at 0, 10, 20 and 40 mg L^{-1} concentrations in deionized water. The resultant solutions were agitated on a water bath shaker using the optimized adsorbent dose at pH 6.0 ± 0.2 for 5 h followed by analysis for the residual Pb^{2+} ions.

2.8. Stability and reusability studies

This desorption study was brought out with 0.1 M of HNO₃ solution. 0.5 g of Pb^{2+} ions loaded on CDs/Al₂O₃NFs nanocomposite after adsorption was dried in the hot air oven. After that CDs/Al₂O₃NFs nanocomposite was mixed into 50 mL of HNO₃ solution and shaken in a shaker at 25 °C for 24 h. Then mixture was collected by using centrifuge at 6000 rpm for 10 min and get CDs/Al₂O₃NFs nanocomposite. The quantity of desorption of Pb^{2+} ions was investigated from the amount of Pb^{2+} ions in aqueous solution.

2.9. LFP detection with Pb^{2+}-CDs/Al₂O₃NFs adsorbent by physical method

Fingerprint detection was carried out using the dusting method with reusable lead loaded adsorbent of Pb^{2+}-CDs/Al₂O₃NFs nanocomposite detecting powder. Firstly, fingerprint donors cleaned their hands with detergent and dried their hands in air. Then the fingers were smoothly rubbed on foreheads and nose and then the thumb impression was applied on various porous and non-porous substrates. Then the labeling powder of Pb^{2+}-CDs/Al₂O₃NFs nanocomposite on dispersed on the fingerprint and the excess labeling powder was cleaned with a squirrel brush. The fingerprint images were captured by a Hisense Phone camera under normal light.

3. Results and discussion

3.1. XPS analysis

XPS measurements were performed to determine the surface elemental characteristics of CDs/Al₂O₃NFs nanocomposite (Qin et al., 2018). Fig. 1(A) shows the XPS spectra of CDs/Al₂O₃NFs nanocomposite which clearly revealed the presence of Al, C and O. Energy bands at 75 eV, 121 eV, 285 eV and 531 eV corresponded to Al 2s, Al 2p, C 1s and O 1s core levels respectively. Fig. 1(B) depicts the deconvolution of the O1s core-level spectrum producing six peaks at 531.25, 532.35, 533.09, 533.86, 534.30, and 534.37 eV corresponding to Al—OH, C—O—Al, C=O, O—C=O and C—O—C/C—OH (Zhang and Chen, 2014). Fig. 1(C) shows the deconvolution of the C1s core-level spectrum producing 5 peaks at 284.69, 289.14, 290.52, 291.92 and 292.89 eV corresponding to C—O, C—C, O=C—O, C=C and C=O (Valdesueiro et al., 2016; Toledo et al., 2018). Fig. 1(D) shows the deconvolution of the Al spectrum, where the Al-OH peak which formed at 77.79 eV revealed the origin of the oxygen peak observed in the wide scan spectrum and Al 2p at 120.61 eV formed from Al₂O₃NFs. Furthermore, the peaks revealed at 120.27 and 122.34 eV corresponded to Al $2p_{3/2}$ and Al $2p_{1/2}$.
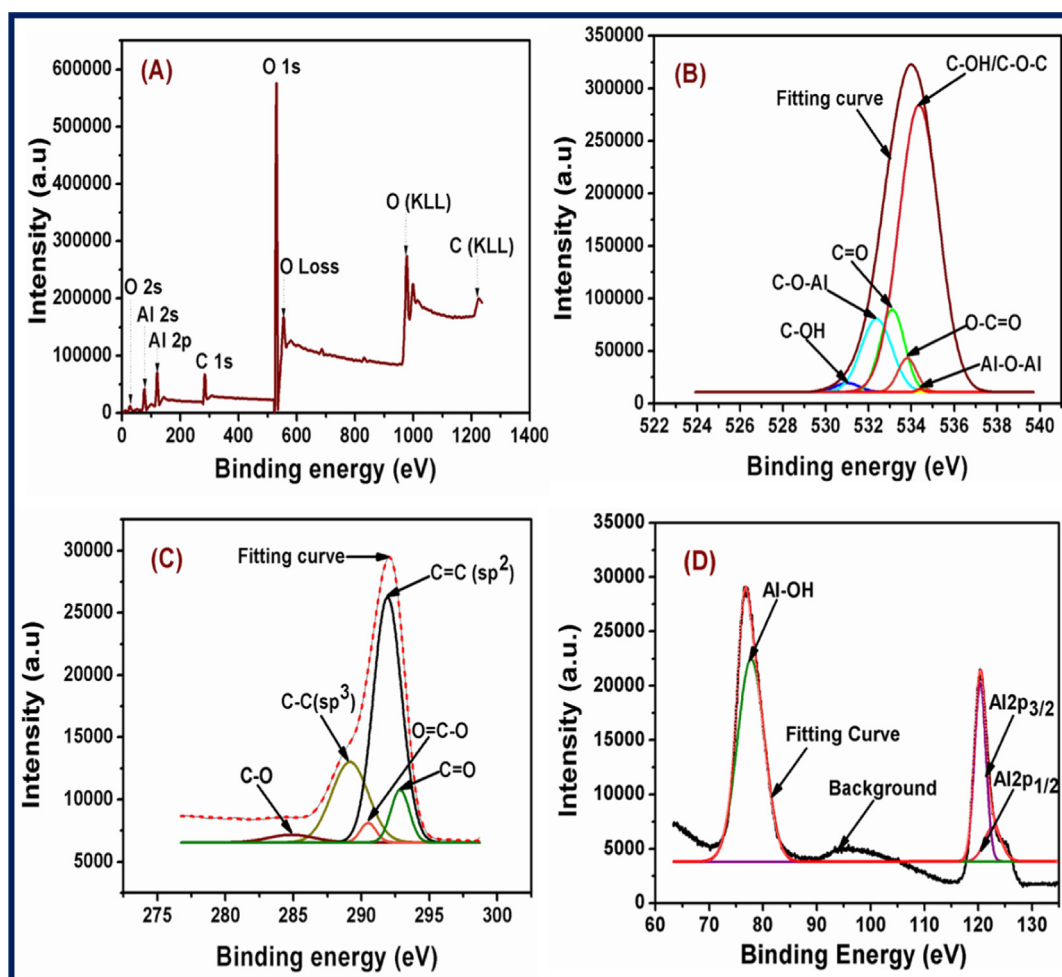
Fig. 1 (A–D) XPS spectra of CDs/Al_2O_3NFs nanocomposite (A) Survey spectrum and Fitting curve of (B) O 1s, (C) C1s and (D) Al.

3.2. Surface morphology analysis

The SEM images of Al_2O_3NFs were displayed at different magnification as shown in (supporting information Fig. S7 (A–D)). The Al_2O_3NFs sheet and particles were observed at a low magnification at 200 μM as shown in (supporting information Fig. S7(A)). The mixing of particles with sheets morphology was recorded at magnification 100 μM as shown in (supporting information Fig. S7(B)). The sheets with crushed particles were clearly indicated at a high magnification of 50 μM with different focus areas as shown in the (supporting information Fig. S7(C&D)). Surface space morphology and the microcrystalline nature of the nanoparticles were characterized by SEM. Fig. 2(A–C) shows the SEM images of CDs/Al_2O_3NFs nanocomposite with various magnifications. The CDs were mixed with Al_2O_3NFs sheets and particles at low magnification 100 μM as shown in Fig. 2(A). The white particles of CDs were clearly deposited on the Al_2O_3NFs at high magnification as shown in Fig. 2(B). The CDs were coated on Al_2O_3NFs with clear images at higher magnification 20 μM as shown in Fig. 2(C). Fig. 2D shows the percentage of elemental composition of CDs/Al_2O_3NFs nanocomposite determined by EDAX. Fig. 3(A–F) shows the (A) mapping image of Pb^{2+}-CDs/Al_2O_3NFs nanocomposite at 25 μm, (B)

Al, (C) C, (D) O, (E) Pb^{2+} ion and (F) SEM image of Pb^{2+}-CDs/Al_2O_3NFs nanocomposite at 10 μm. The above data confirmed the binding of Pb^{2+} ions after adsorption on the surface of CDs/Al_2O_3NFs nanocomposite.

3.3. Transmission electron microscopy characterization

The size and shape of Al_2O_3NFs were determined by TEM with corresponding images were observed at different magnification 200 nm, 100 nm and 50 nm as shown in (supporting information Fig. S8(A–C). The compact nature of Al_2O_3NFs was recorded at low magnification of 200 nm as shown in (supporting information Fig. S8(A)). The network of Al_2O_3NFs image was clearly observed at a high magnification of 100 nm as shown in (supporting information Fig. S8(B). The highest magnification of 50 nm gave better images of Al_2O_3-NFs as shown in Fig. S8(C). The TEM images indicate that the Al_2O_3NFs was obtained at 500 °C due to the alumina nanofibers consisting thermal stability materials (Zhang et al., 2016a, 2016b; Li et al., 2016a, 2016b; Lu et al., 2012). Fig. S8(D) shows the specific diffraction patterns which indicate the crystallinity of the Al_2O_3 nanofibers as shown by the white ring on SEAD image. The synthesized CDs were also subjected to TEM analysis and its images are shown in
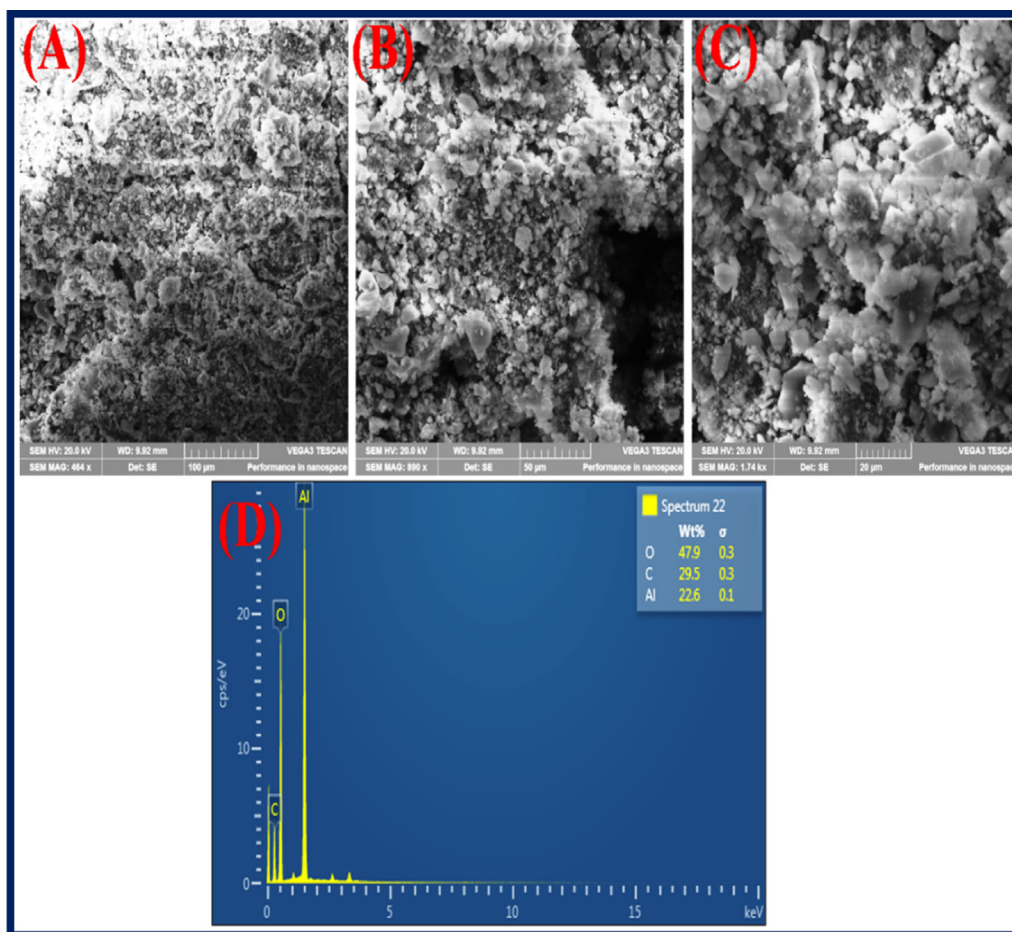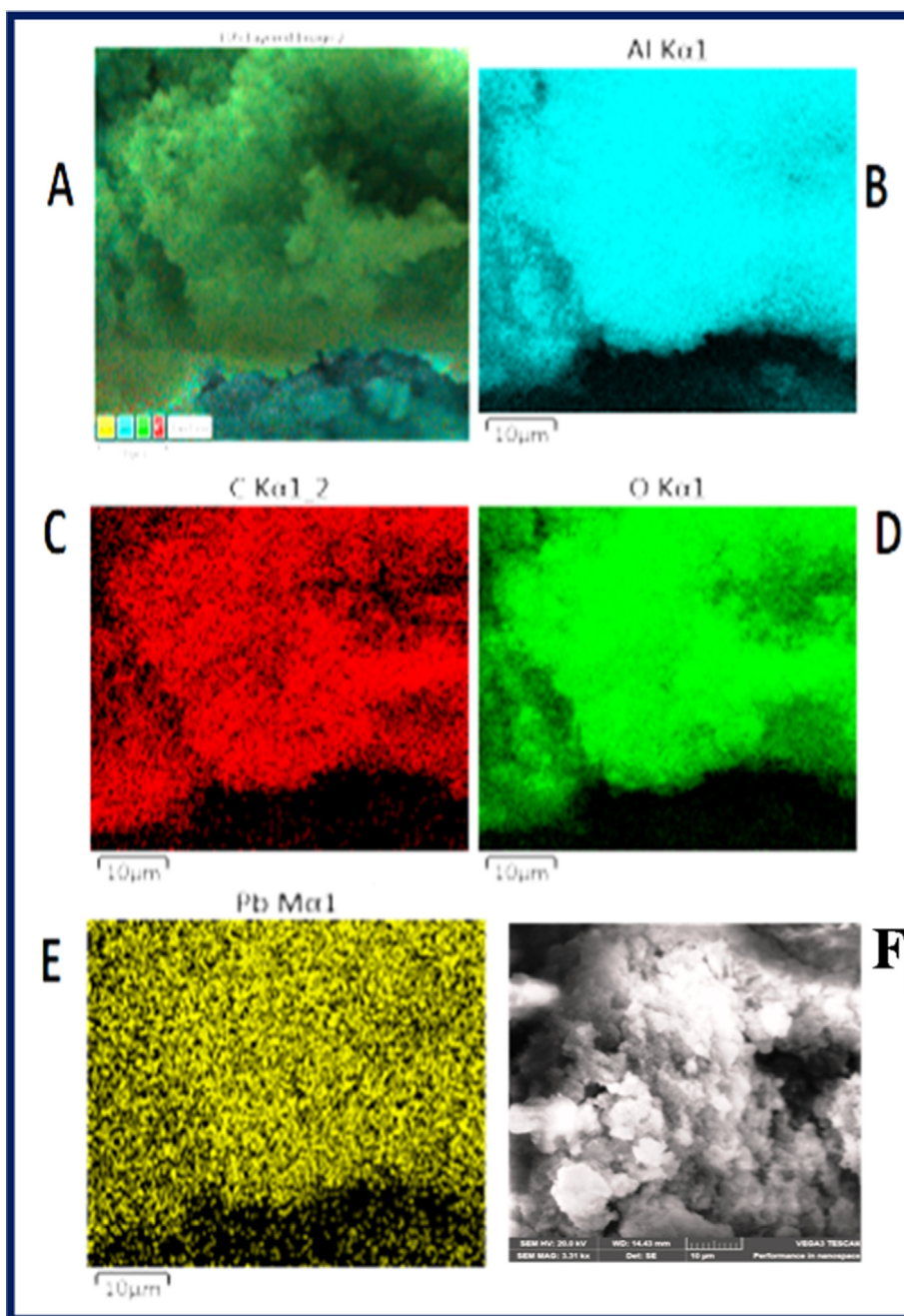
Fig. 2 (A–D) SEM images of CDs/Al₂O₃NFs nanocomposite at different magnifications of (A) 100 μM, (B) 50 μM, (C) 20 μM and (D) EDAX.

Fig. 4(A–D). At a low magnification of 200 nm, CDs was displayed merged images as shown in Fig. 4(A). The dots and spherical shape of CDs were observed at a higher magnification 100 nm as shown in Fig. 4(B&C). The highest magnification of 50 nm, showed the spherical image of CDs as shown in Fig. 4(D). The average size of CDs (51.18 nm) was calculated from plot of diameter vs frequency as shown in Fig. 4(E). This result correlated with the XRD patterns of CDs (Zhang et al., 2016a, 2016b; Alam et al. 2015; Prabakaran and Pillay 2020). Fig. 5(A–D) shows the TEM images of the CDs/Al₂O₃NFs nanocomposite at magnifications of 200 nm, 100 nm and 50 nm. CDs coated on Al₂O₃NFs were observed at low magnification as shown in Fig. 5(A). The black dots indicate that CDs were deposited on Al₂O₃NFs and this image was observed at a high magnification of 100 nm as shown in Fig. 5(B). The CDs coated on Al₂O₃NFs were clearly displayed at the highest magnification 50 nm and also CDs on Al₂O₃ NFs are marked with yellow circles as shown in Fig. 5C. The TEM images confirmed that the CDs were coated on Al₂O₃NFs (Liu et al., 2013). The bright circle observed on the SEAD patterns was due to the increase in the crystallinity of Al₂O₃ NFs as shown in Fig. 5D.

3.4. Batch adsorption studies

3.4.1. Effect of adsorbent dosage

The effect of adsorbent dosage on the adsorption of Pb^{2+} from aqueous solution (20 mg L^{-1}), was studied by varying the adsorbent mass from 0.1 g–0. 6 g at pH 6 with a contact time of 6 hr as shown in Fig. 6A. The percentage removal of Pb^{2+} increased with increasing adsorbent dosage and rapidly dropped at 0.30 g due to more masses of the adsorbent CDs/Al₂O₃NFs nanocomposite in lower concentration of Pb^{2+} ions solution. It was observed that the maximum percentage removal of Pb(II) occurred at 100% at 0.2 g because of the number of binding sites available and optimum dosage of CDs/Al₂O₃NFs nanocomposite as shown in Fig. 6A. Further, increases of adsorbent dosage corresponding to masses of 0.4 g, 0.5 g and 0.6 g only slightly increased the percentage of removal of Pb^{2+} ions due to the number of ions bound to the adsorbent and the number of free ions remains constant as shown in Fig. 6A. This data showed that the optimum dosage of CDs/Al₂O₃NFs nanocomposite adsorbent at 0.20 g with 100% maximum removal percentage.

Fig. 3 (A–F) Elemental mapping for Pb^{2+}-CDs/Al_2O_3NFs nanocomposite (A) mapping image at 25 µm, (B) Al, (C) O, (D) C, (E) Pb^{2+} ions and (F) SEM image of CDs Pb^{2+}-CDs/Al_2O_3NFs nanocomposite at 10 µm.

3.4.2. Effect initial concentration of Pb^{2+} ions

Fig. 6B shows the dependence of the adsorption process of Pb^{2+} ions adsorption on different initial concentration from 0 to 80 mg L^{-1} with CDs/Al_2O_3NFs nanocomposites. The experiments were achieved using 20 mL of Pb^{2+} ions solution with different initial concentrations as mentioned above at pH 6 for CDs/Al_2O_3NFs nanocomposites. The percentage of adsorption removal was increased with increasing concentration of Pb^{2+} ions from 0 to 20 mg L^{-1} and removal of Pb^{2+} ions decreased with higher concentration of 30–40 mg L^{-1} as shown in Fig. 6B. At lower concentration of Pb^{2+} ions, the number of Pb^{2+} ions which are available in the solution is less

as compared to the available sites on the adsorbent. However, at higher concentrations, the available sites for adsorption become fewer and the percentage removal of Pb^{2+} ions depends on the initial concentration. The maximum percentage removal of Pb^{2+} ions was obtained at 20 mg L^{-1} with 100% for CDs/Al_2O_3NFs nanocomposite as adsorbents as shown in Fig. 6B.

3.4.3. Effect of pH

Different pH (1 to 9) of the Pb^{2+} solutions was investigated for maximum removal efficiency of CDs/Al_2O_3NFs nanocomposite as shown in Fig. 6C. The highest percentage removal of
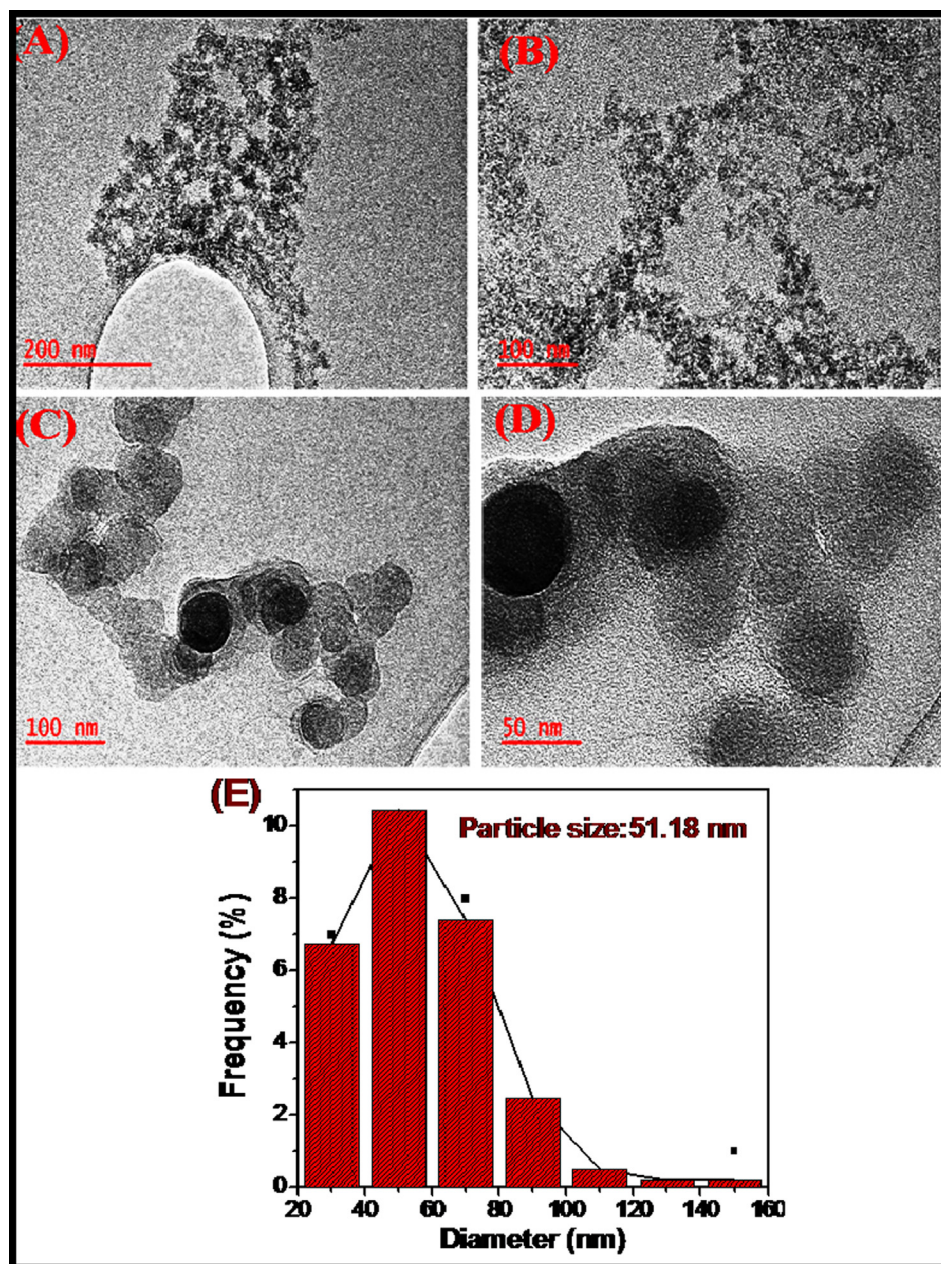
Fig. 4 (A–E) TEM of CDs at (A) 200 nm, (B & C) 100 nm, (D) 50 nm and (E) Histogram plot of particles size distribution.

Pb^{2+} ion was observed at pH 6.0. In the acidic range Pb^{2+} ions compete with H$^+$ ions for active adsorption sites on CDs/Al$_2$O$_3$NFs nanocomposite (Iqbal et al., 2013; Reddy et al., 2012). Lower removal percentages were noted at higher pH (7 to 9) because of the precipitation of Pb(OH)$_2$ from Pb^{2+} ions and the negative surface charge of CDs/Al$_2$O$_3$NFs nanocomposite. pH 6.0 was therefore identified as the optimum pH for the adsorption activity of CDs/Al$_2$O$_3$NFs nancomposite as shown in Fig. 6C. The CDs/Al$_2$O$_3$NFs nanocomposite has exhibited a higher point of zero charges because of CDs coated on Al$_2$O$_3$NFs and also increases adsorption of the capacity of Pb^{2+} ions. Above pH 5.5 of there is increased adsorption of Pb^{2+} ions because of electrostatic interactions of the negative charge of CDs/Al$_2$O$_3$NFs

nanocomposite and positive charge of Pb^{2+} ions. Below pH 5.5 the adsorption of Pb^{2+} ions was not significant due to the electrostatic repulsion of the positive charge of CDs/Al$_2$O$_3$-NFs nanocomposite and positive charge of Pb^{2+} ions.

3.4.4. Effect of contact time

Effect of contact time was used to determine the adsorption capacity of the CDs/Al$_2$O$_3$NFs nanocomposite at different time interval ranges of 60 to 360 min as shown in Fig. 6D. The experiments were carried out using 20 mL of Pb^{2+} ions with 20 mg L^{-1} of CDs/Al$_2$O$_3$NFs nanocomposite at pH 6 with an agitation speed of 200 rpm at room temperature. The rate of adsorption of Pb^{2+} ions by the CDs/Al$_2$O$_3$NFs nanocomposite was 90% within 60 min. Then adsorption
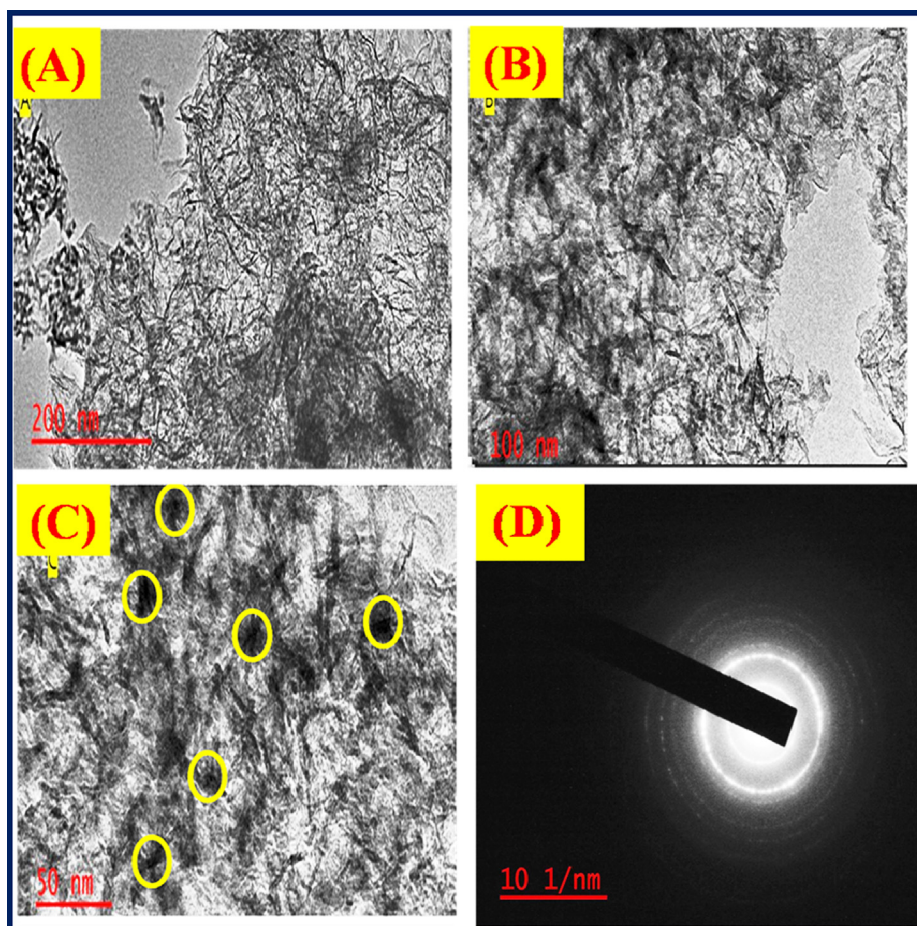
Fig. 5   (A–D) TEM images of CDs/Al$_2$O$_3$NFs nanocomposite (A) 200 nm, (B) 100 nm, (C) 50 nm and (D) SAED pattern.

decreased and increased again. The equilibrium time was observed at 300 min. The maximum percentage removal of Pb^{2+} ions by CDs/Al$_2$O$_3$NFs nanocomposites was 99.87%.

3.4.5. Adsorption isotherm studies

The sorption characteristics were assessed by plotting both the Langmuir and Freundlich isotherms. The Langmuir adsorption isotherm study was evaluated the absorption efficiency of CDs/Al$_2$O$_3$NFs nanocomposite as per the following Langmuir Eqs. (4) and (5) given below.

$$\frac{C_e}{q_e} = \frac{C_e}{q_e} + \frac{1}{bq_o} \tag{4}$$

Eq. (3) above can be represented as:

$$\frac{1_e}{q_e} = \frac{1_e}{bq_m c_e} + \frac{1}{q_o} \tag{5}$$

where C_e (mg L^{-1}) is the equilibrium concentration, q_e (mg g^{-1}) is the adsorption amount in equilibrium, qo is the maximum adsorption amount, and b is the Langmuir constant related to adsorption capacity and energy of adsorption. For the Langmuir isotherm, $1/qe$ is plotted against $1/C_e$ as shown in (supporting information Fig. S9(A)). The maximum adsorption capacity q$_m$ for Pb^{2+} ions was found to be 14.28 mg g^{-1} at 25 °C. In order to determine whether adsorption was favorable

or not, the dimensionless factor r was considered and it can be calculated as described in Eq. (6):

$$r = \frac{1}{(1 + b.c_0)} \tag{6}$$

where b is the Langmuir's constant and c is the initial concentration of Pb^{2+}. The calculated value of separation factor 'r' at different initial concentration was found in the range of −0.06 to −10. If the value of r is less than 1, the adsorption is favorable; if r is greater than 1, the adsorption is not favorable; and r is 0 the adsorption is irreversible (Sen et al., 2010; Iqbal et al., 2009). Based on this, the adsorption in this study was favorable since r found was less than 1.

The multilayer adsorption isotherm of CDs/Al$_2$O$_3$NFs nanocomposite was determined by the Freundlich adsorption isotherm. The Freundlich's equation can be written as Eq. (7)

$$\log q_e = \log K_f + \frac{1}{n}\log C_e \tag{7}$$

where K_f is the Freundlich's constant related to bisorption capacity and n is the Freundlich's constant related to bisorption intensity. The biosorption intensity n can be used as follows. If $n = 1$ is linear adsorption, if $n < 1$, the adsorption is a chemical process and if $n > 1$, adsorption is a physical process (Ali and Gupta, 2006). The value of n was less than 1 which was obtained from slope of plot log qe is plotted against logC_e as shown in (supporting information Fig. S9(B)). This
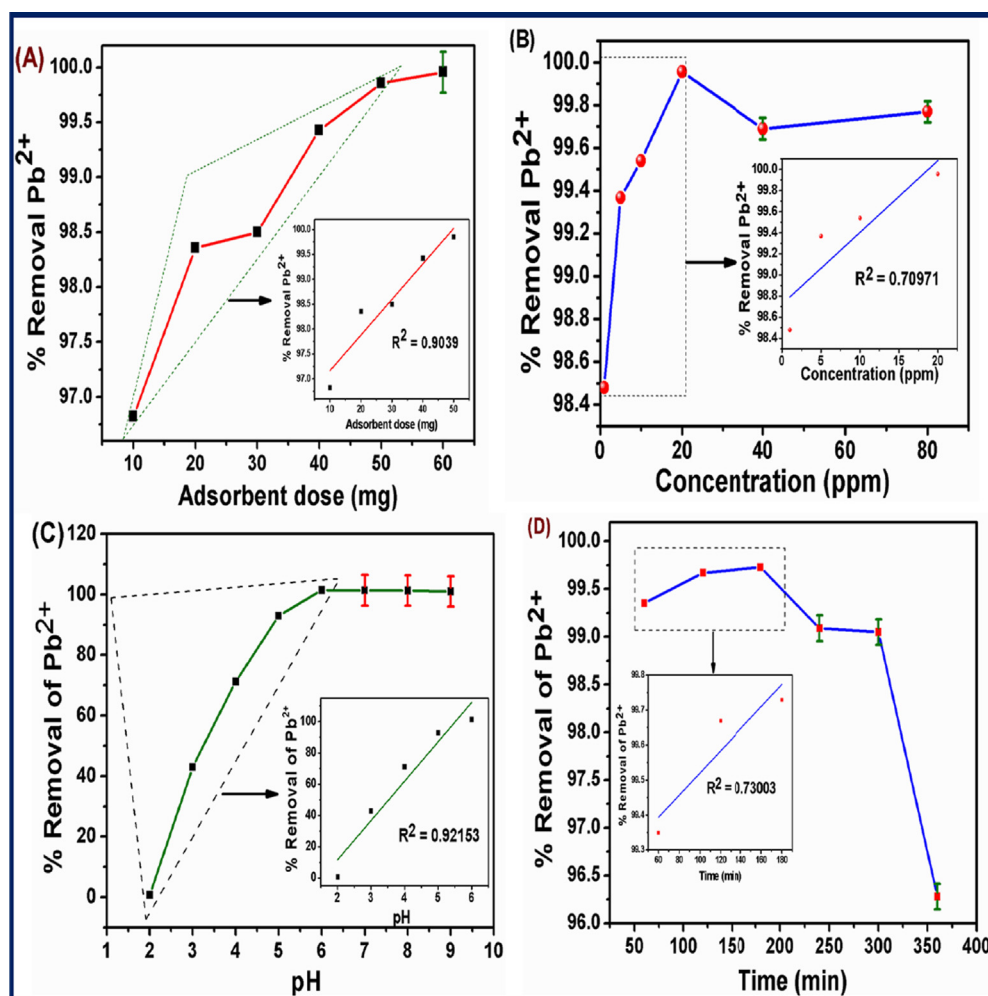
Fig. 6 (A–D) (A) Effect of dosage and (B) effect of concentration using 0.2 g CDs/Al₂O₃NFs nanocomposite, 20 mg L^{-1} of 20 mL Pb^{2+} solution, at 25 °C; pH 6, for 5 h at 200 rpm, (C) Effect of pH using 0.2 g CDs/Al₂O₃NFs nanocomposite, 20 mg L^{-1} 20 mL of Pb^{2+} solution, pH 1 to pH 9 at 25 °C for 5 h at 200 rpm and (D) Effect of contact time using 0.2 g CDs/Al₂O₃NFs nanocomposite, pH 6, 20 mg L^{-1} of 20 mL Pb^{2+} solution, at 25 °C for 60 to 360 min at 200 rpm. Error bars correspond to standard deviation of triplicate measurements.

Table 1 Adsorption isotherm models parameter for adsorption of Pb^{2+} ions by CDs/Al₂O₃NFs nanocomposite at 25 °C.

Langmuir isotherm		Freundlich isotherm	
q_m (mg/g)	14.28	K_F (L/g)	177.83
B (L/g)	1.4×10^{-3}	n	0.59
r value	0.90–0.99	R^2	0.98
R^2	0.96		
Dubinin–Radushkevich		**Temkin isotherm**	
β (mol²/Kj²)	2.76×10^{-8}	B_T	0.29
q_m (mg/g)	1.13	K_T (L/g)	3.682
R^2	0.91	R^2	0.86
Toth isotherm			
K_t (mg/g)	3.09		
a_t (L/mg)	3.36		
R^2	0.80		

parameters were summarized as shown in Table 1. It was observed that the adsorption followed Freundlich model since it had a better correlation than Langmuir model. Further, maximum bisorption capacity range of (177.83 mg g^{-1}) CDs/Al₂O₃NFs nanocomposite was compared with other adsorbents as shown in Table 2.

Dubinin–Radushkevich (D-R) Isotherm

Dubinin–Radushkevich (D-R) isotherm model was fitted to the adsorption data as shown in the supporting information Fig. S9(C). This clearly depicts the adsorption process and also calculates the mean free energy of the adsorption method (Hutson and Yang, 1997). The linear form of the D-R isotherm is given by Eq. (8)

$$D-R \quad lnqe = lnq_m - be^2 \tag{8}$$

value was also evident from chemical adsorption processes. And also Langmuir and Freundlich adsorption isotherm

$$\varepsilon = RT \ ln[1 + \frac{1}{C_e}] \tag{9}$$

Table 2 Comparative evaluation of Pb^{2+} ions adsorption capacity of CDs/Al_2O_3NFs nanocomposites with other reported adsorbents at 25 °C.

Adsorbent	Isotherm Model	Maximum adsorption capacity (mg g^{-1})	References
Fe_3O_4, ZnO, and CuO nanoparticles	Freundlich isotherm	30.310, 50.00, 2.95	Mahdavi et al., 2012
CNT/MnO_2	Langmuir	82.6	Wang and Ariyanto, 2007
CNT/Al_2O_3	Langmuir	67.11	Hsieh and Horng, 2007
Polypyrrole-Polyaniline/Fe_3O_4	Langmuir	243.9	
ZnO@Chitosan core/organically shell nanocomposite	Langmuir	476.1	Saad et al., 2018
CDs/Al_2O_3NFs nanocomposite	Freundlich isotherm	177.83	Current work

From the adsorption equation of (8) and (9), where k_D and ε are D-R constant (mol^2 kJ^{-2}) and D-R isotherm constant, respectively; R and T are the gas (8.314×10^{-3} kJ mol^{-1} K^{-1}) and temperature (K) constant, respectively and q_s is the saturation capacity (mg g^{-1}). The parameter was obtained by the linear plots of ln q_e vs. ε^2. The mean free energy, E (kJ mol^{-1}) is obtained from k_D and is expressed as follows:

$$E = \frac{1}{\sqrt{2\beta}} \tag{10}$$

Hereby, the mean adsorption energy was found to be 4.257 kJ mol^{-1}. This amount *(E)*, obtained from the D–R model, is useful for it provides us with information about the mechanisms of adsorption process. If the *E* value is between 8 and 16 kJ mol^{-1}, the type of adsorption process is chemical; however, if $E < 8$ kJ mol^{-1}, the process occurs physically.

Temkin isotherm

The Temkin isotherm was also applied for the linear fit of adsorption experimental results just like the Langmuir and Freundlich equations as shown in (supporting information Fig. S9(D)). This Temkin isotherm was fitted to explain the interaction of the adsorbent and Pb^{2+} adsorption and also is dependent on the free energy of adsorption with adsorbent surface coverage (Saruchi, 2019). Temkin isotherm linear model was described with Eq. (8)

Temkin $\quad q_e = B \; ln k_T + B \; ln Ce \tag{11}$

where Temkin isotherm constants B of slope and k_T of intercept (kJ mol^{-1}) were obtained from plot of q_e versus $lnCe$. Temkin parameters are given in Table 3.

Toth adsorption isotherm

The Toth isotherm describes the site affinities and is based on the Langmuir adsorption isotherm as shown in (supporting information Fig. S9(E)). The Toth isotherm linear equation is given below

$$ln(q_e/k_t) = lnC_e - 1/t \hat{A} \cdot ln(a_t + C_e) \tag{12}$$

where the Toth model constant is K_t, qe is the amount adsorbed at equilibrium (mmol g^{-1}), and C_e is the equilibrium concentration and a is a constant for binding attraction and accurate to adsorbate-adsorbent interaction (kPa^{-1}) and t is dependent to surface heterogeneous and it was lower or equal to unity. The t value is unity and also adsorbent as homogeneous adsorption activity (Toth 1971). The parameters of the Toth adsorption isotherm are shown in Table 3.

Fig. S9F(a–e) shows the fitting of experimental data for various concentrations of Pb^{2+} ions using the non-linear models of Langmuir, Freundlich, Dubinin-Radushkevich, Temkin and Toth isotherm models as shown in Eqs. (13)–(17) below. These models are based on the relationship between equilibrium concentration and adsorption capability. These adsorp-

Table 3 Adsorption isotherm models non-linear parameter for adsorption of Pb^{2+} ions by CDs/Al_2O_3NFs nanocomposite.

Parameters	Langmuir	Freundlich	Tempkin	Toth	D-R
$q_m (mgg^{-1})$	0.78			1.79	0.89
K_F		1.09			
K	1.23				
n		0.233		1.07	
K_T			1.09	1.76	
B			1.21		
E					2.878
R^2	0.9993	0.9994	0.9989	0.9993	0.9860

tion models separately predicted the accuracy of adsorption activity.

Langmuir

$$q_e = \frac{q_m K C_e}{1 + K C_e} \tag{13}$$

Freundlich isotherm model

$$q = K_F (C_e)^{1/n} \tag{14}$$

Tempkin isotherm model

$$q = B \ln(K_T C_e) \tag{15}$$

Dubinin–Radushkevich (D–R) isotherm

$$q_e = q_m \exp\left(\frac{(RT\ln(1 + 1/C_e))^2}{-2E^2}\right) \tag{16}$$

Toth isotherm model

$$q_e = \frac{q_m C_e}{[(K_T + C_e^n)]^{1/n}} \tag{17}$$

where Qe is equilibrium solid phase concentration (mg/g) and Ce is equilibrium liquid phase concentration (mg/L) in all isotherm models. In all models, Q_m parameter is relevant with adsorption capacity. In the Freundlich isotherm model K_f and n are isotherm parameters characterizing adsorption capacity and intensity, respectively. In the Langmuir equation K_L and a_L are the Langmuir constants related to the adsorption capacity and energy of adsorption, respectively. In the D-R isotherm, E is energy of adsorption. In the Tempkin isotherm K_T is equilibrium binding constant (L/g), b is related to heat of adsorption (J/mol), R is the gas constant (8.314×10^{-3} kJ/K mol) and T is the absolute temperature (K). K_{To} is the Toth model constant and n the Toth model exponent ($0 < n \leq 1$).

Fig. S9F (a–e) displays the fitting of the experimental adsorption data with the shown isothermal equilibrium models. The capacity of adsorption was dependent upon the initial concentration of Pb²⁺ ions. Increased initial concentration of Pb²⁺ often increases equilibrium adsorption due to changes in the mass driving force in the adsorption solution with a rise in initial concentration. The increase in driving force was related to the solution adsorption of Pb²⁺ ions. The rise in the mass driving force allows more Pb²⁺ ions to diffuse into the adsorbent structure from the liquid phase, thereby resulting in higher adsorption capacity. Sigmoidal-shaped isotherm models were obtained with non-linear plots. This means that the activation energy for desorption of Pb²⁺ is concentration-dependent (Sadeghi Pouya et al., 2015; Alberti et al.,2012; Giles et al., 1974). From the experimental results with higher R² values, the Freundlich, Langmuir, Dubinin –Radushkevich isotherm models were better suited than other models, and also all model parameters are shown in Table 3. From the various R² values reported in Table 1 and Fig S9 it was evident that the Langmuir Isotherm Model provided the best fit to the experimental data hence the adsorption process was governed by a monolayer homogeneous adsorption.

3.4.6. Effect of competing ions

In general, several ions are present in natural and wastewater. In this study divalent ions such as Ni²⁺, Cu²⁺, Cd²⁺, Mn²⁺, Fe²⁺ along with Pb²⁺ ions might compete for binding sites
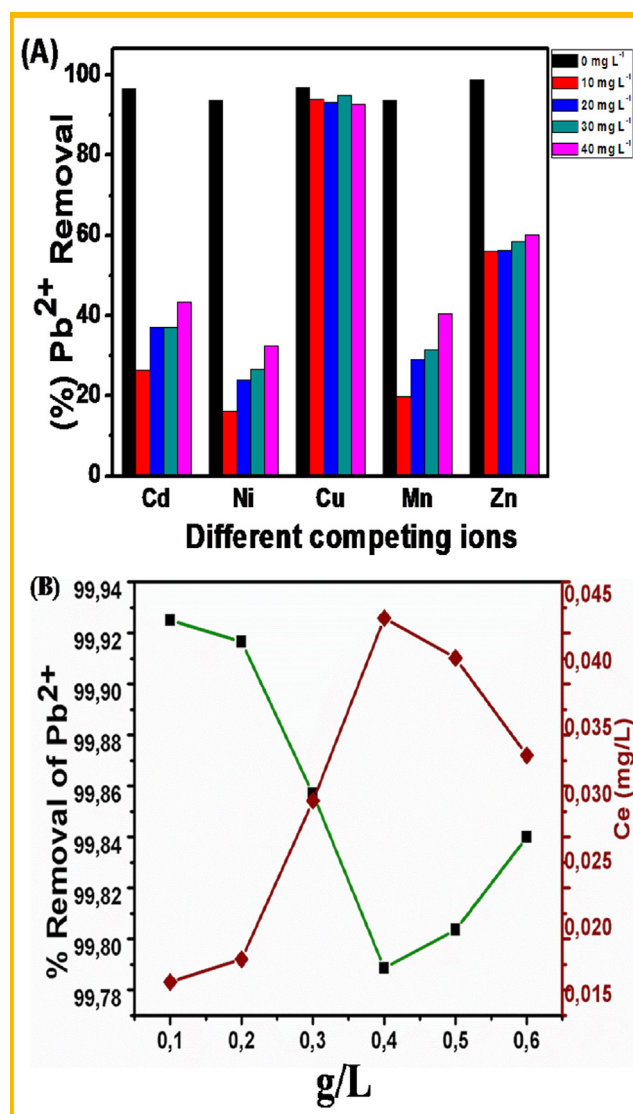

Fig. 7 (A&B) (A) Effect of competing ions and (B) Application on real water sample onto the Pb²⁺ with CDs/Al₂O₃NFs nanocomposite.

which will then interfere with Pb²⁺ adsorption (Zhu et al., 2015; Fifi et al., 2013; Kosa et al., 2012). It was therefore important to study the effect of the various above-mentioned ions on Pb²⁺ ions removal efficiency by CDs/Al₂O₃NFs nanocomposites. Although all these ions are divalent they all interact with different capacities at the surface of CDs/Al₂O₃ nanocomposites (Chigondo et al., 2018). The initial concentration of Pb²⁺ ions was kept constant at 1 mg L⁻¹ whilst that of interfering ions was varied from 0 to 40 mg L⁻¹ and pH adjusted to 6, mechanism adjusted from Chigondo and co-workers (Mubarak et al., 2016). The results indicate that Cd²⁺, Ni²⁺, Cu²⁺, Mn²⁺, Zn²⁺ caused a decrease in Pb²⁺ ions adsorption for all concentration from 0 to 40 mg L⁻¹. Ni²⁺ had the greatest impact on Pb²⁺ ions adsorption decreasing from 93.72 to 16.22% as shown in Fig. 7(A). Hence the interference order was as follows: Ni²⁺ > Mn²⁺ > Cd²⁺ > Zn²⁺ > Cu²⁺. This is related to the formation of inner and outer sphere complexes associated with the different ions.

Although many studies in ions competing with binding sites on a specific adsorbent were explored, there is still a lack of understanding the order of binding of heavy metals ions by carbon nanoparticles coated on Al_2O_3NFs. Mubarak and co-workers (2014) (Lasheen et al., 2015) studied the Removal of Pb^{2+} ions from Wastewater Using Carbon Nanotubes and found that the affinity for metal ions was $Cu^{2+} > Pb^{2+} > Co^{2+} > Zn^{2+} > Mn^{2+}$, Lasheen et al. (2013) (Lenntech 2019) studied the Removal of heavy metals from aqueous solution by multiwalled carbon nanotubes and found that $Pb^{2+} > Cu^{2+} > Cd^{2+} > Ni^{2+}$. From the previous studies it can be seen that the interference order of ions on the binding site differs from adsorbent to adsorbent which depends on the properties of the individual ions. Furthermore, the order of interfering ions could depend on charge per radius value (Z/R). The higher the charge to radius value, the higher the ion is attracted to the binding site of the adsorbent. Ni^{2+} (2/0,70) which is the same as Mn^{2+} (2/0,70) This explained why their interference is higher than the other ions present as shown in figure. The trend did not continue for Cu^{2+} (2/0, 73), Zn^{2+} (2/0, 74), Cd^{2+} (2/0, 95). This could be explained by some inner sphere complexation for Cd^{2+}. Fig. 7 (A) shows that Cu^{2+} interferes less than the other ions present.

3.4.7. Application on industrial wastewater sample

To assess the Pb^{2+} ions removal efficiency of CDs/Al_2O_3NFs nanocomposite in industrial wastewater, a water sample from Doornkop plant (−26.201351, 27.773653) in Randfontein, Johannesburg, South Africa whose source is from mine and sewage was collected and stored under cool conditions. The pH found was 7.8 and concentration of Pb^{2+} ions in water was 13.97 µg L^{-1} which falls within the range as described in a previous report (Cao et al., 2012). The Pb^{2+} ions concentration was spiked to a concentration of 20 mg L^{-1} and the new pH found was 6.61 which were then brought to it to approximately pH 6. Furthermore this prepared industrial wastewater was brought into contact with doses of CDs/Al_2O_3NFs nanocomposite ranging from 0.1 to 0.6 g in 20 mL. An increase in adsorbent dosage resulted in rapid removal of Pb^{2+} ions at 0.1 g to 99.93% and then a decrease of Pb^{2+} ions removal was observed until 0.4 g dosage. Then an increase in Pb^{2+} ions removal followed until 0.6 g dosage. Furthermore, an increase in Pb^{2+} ions equilibrium concentration was observed as the adsorbent dosage increased until 0.4 g then afterwards a decrease in concentration equilibrium was observed as shown in Fig. 7(B). CDs/Al_2O_3NFs nanocomposites has proven to be capable of reducing Pb^{2+} ions level to about 15 µg L^{-1}, value which is well below the limit of 15 mg L^{-1} as recommended by EPA and WHO.

3.4.8. Adsorption mechanism of Pb^{2+} ions with CDs/Al_2O_3NFs nanocomposite
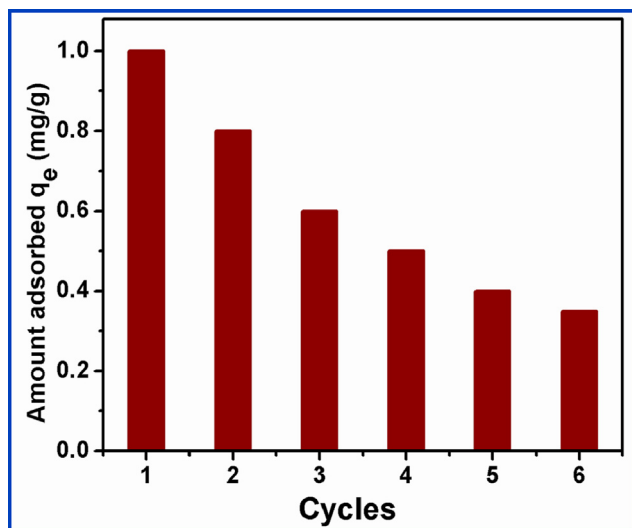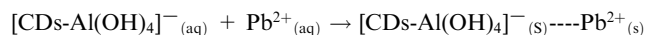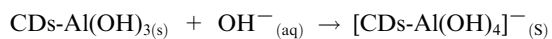
In order to understand the adsorption mechanism, pH and ion exchange was considered. Surface hydroxyl groups are mainly reported to be involved in the ion exchange process during anion adsorption (Chen et al., 2012). However, such an ion exchange mechanism does not work for cation adsorption because cations and hydroxyl groups have opposite electric charge. The pH of the solution at the end of the experiment decreased after adsorption by CDs/Al_2O_3NFs nanocomposites which indicated a possible mechanism by which Pb^{2+} was adsorbed onto CDs/Al_2O_3NFs nanocomposite involved a cations exchange of Pb^{2+} with H^+. From the ionic exchange principle, the more Pb^{2+} is adsorbed, the more H^+ ions are released hence pH decreases. Furthermore, the point of zero charge was considered (pH_{pzc} = 5.5). As seen in Fig. 5G, the adsorption is efficient at pH 2–6 with pH optimum at 6 after it sharply decreases and becomes constant. When pH < pH_{pzc}, the surface of the CDs/Al_2O_3NFs nanocomposites is more positive with protonation taking place. This leads to Pb^{2+} repulsion and making adsorption not favorable. Adsorption can only take place by cation exchange reaction. When pH > pH_{pzc}, the surface of CDs/Al_2O_3NFs nanocomposite becomes more negative which is favorable for Pb^{2+} adsorption with $Pb(OH)_2$ precipitating. The possible reactions are shown below and the detailed mechanism in Scheme 4.

Ion-Exchange-reaction

$$[CDs\text{-}AlOH]_{(s)} + Pb^{2+}_{(aq)} \rightarrow [CDs\text{-}AlO\text{-}Pb]^{+}_{(aq)} + H^{+}_{(aq)}$$
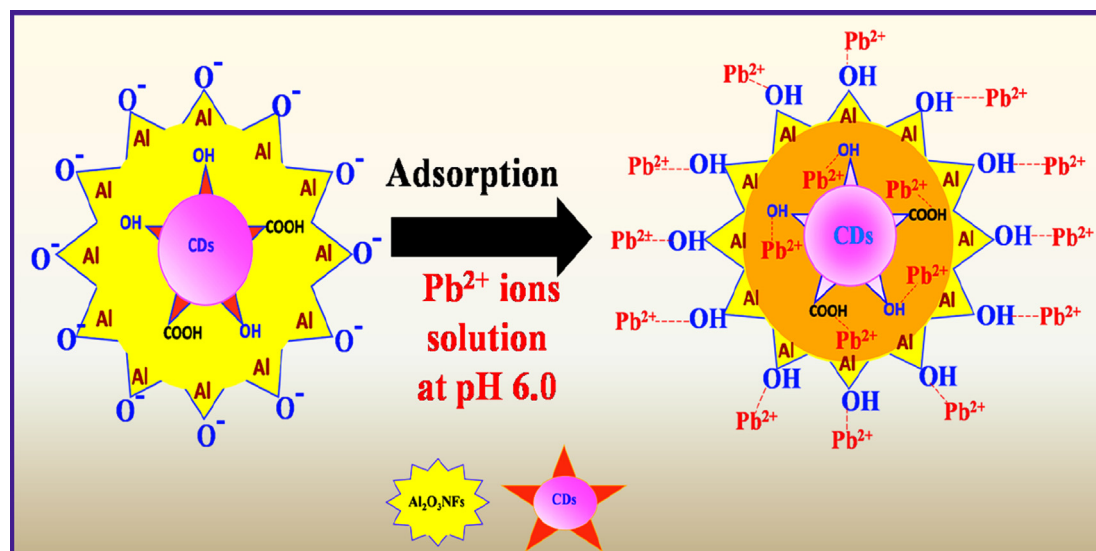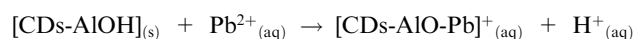
Scheme 4 Adsorption mechanism of Pb^{2+} ions by using CDs/Al_2O_3NFs nanocomposite.

Electrostactic attraction

$$CDs-Al(OH)_{3(s)} + OH^-_{(aq)} \rightarrow [CDs-Al(OH)_4]^-_{(S)}$$

$$[CDs-Al(OH)_4]^-_{(aq)} + Pb^{2+}_{(aq)} \rightarrow [CDs-Al(OH)_4]^-_{(S)}----Pb^{2+}_{(s)}$$

3.4.9. Recycling and stability studies

Recycling and stability were tested for the removal of Pb^{2+} ions from wastewater samples with an adsorbent of CDs/Al$_2$O$_3$NFs nanocomposite. The adsorption of Pb^{2+} ions on nanocomposite CDs/Al$_2$O$_3$NFs was inhibited at pH < 6 when treated with acid to regenerate the adsorbent. Therefore 0.1 M HNO$_3$ was used for the desorption process with 6 cycles of adsorption–desorption. After 6 cycles of adsorption–desorption, the adsorption efficiency decreased as shown in Fig. 8. After 6 cycles, the adsorption capacity decreased from 177.80 to 140.5 mg/g. The removal efficiency of CDs/Al$_2$O$_3$NFs nanocomposite was 63.3% when compared to the first cycle. Thus the lifecycle of CDs/Al$_2$O$_3$NFs nanocomposite as an adsorbent is not indefinitely viable and the reusability of the lead-loaded adsorbent must be explored so as to avoid secondary environmental pollution caused by disposal of the spent adsorbent. As indicated above in this study its reusability as a labeling agent for latent fingerprint detection was examined.

3.4.10. LFP detection by using reusable Pb^{2+}-CDs/Al$_2$O$_3$NFs nanocomposite

Reuse of the metal loaded adsorbent was conducted to avoid secondary pollution and in trying to solve crime that the world in general and South Africa precisely faces. Latent fingerprint
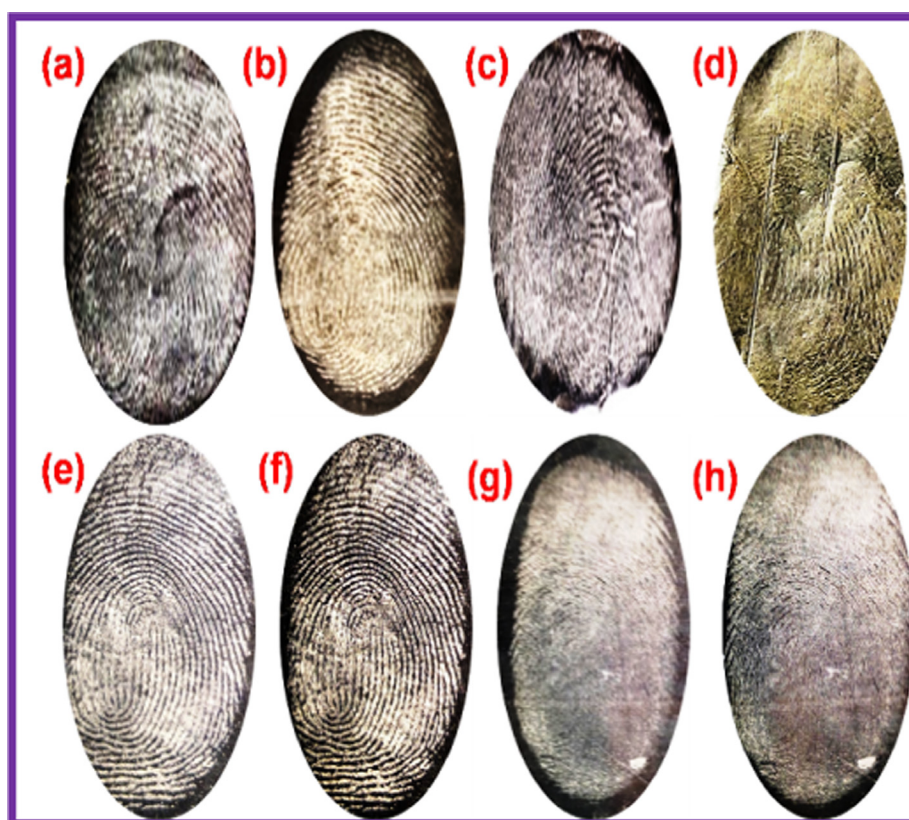

Fig. 8 Difference of the adsorption capacity of CDs/Al$_2$O$_3$NFs nanocomposite for Pb^{2+} ions with adsorption–desorption 6 cycles.

Fig. 9 (a–h) Latent fingerprints images on the different surface materials of glass slide: (a) Al$_2$O$_3$NFs, (b) Pb^{2+}-CDs/Al$_2$O$_3$NFs nanocomposite; aluminium foil: (c) Al$_2$O$_3$NFs, (d) Pb^{2+}-CDs/Al$_2$O$_3$NFs nanocomposite; aluminium sheet: (e) Al$_2$O$_3$NFs, (f) Pb^{2+}-CDs/Al$_2$O$_3$NFs nanocomposite; aluminium rod: (g) Al$_2$O$_3$NPs, (h) Pb^{2+}-CDs/Al$_2$O$_3$NFs nanocomposite under daylight.
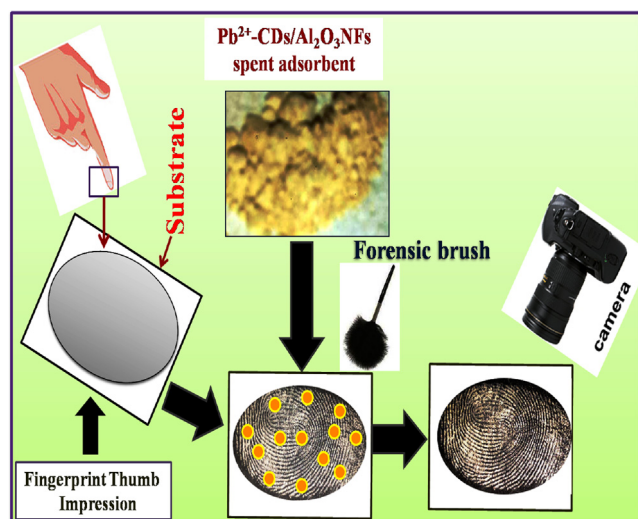
Scheme 5 LFP detection mechanisms with Pb^{2+}-CDs/Al_2O_3-NFs nanocomposite by using powder dusting method.

(LFP) images were developed on various non-porous surfaces which include aluminium foil, aluminium sheets, aluminium rod, and glass slide with corresponding labeling agents of Al_2O_3NFs, Pb^{2+}-CDs/Al_2O_3NFs nanocomposite respectively, under daylight as shown in Fig. 7(a–h). CDs/Al_2O_3NFs nanocomposite gave better images than Al_2O_3NFs on the aluminium sheet as displayed in Fig. 9(f). The images in Fig. 9(a, c, e, g) reveals that Al_2O_3NFs had fair images on the nonporous surfaces. Based on this comparison Pb^{2+}-CDs/Al_2O_3NFs nanocomposite proved to be the best labelling agent powder because of the well-defined images with better fingerprint ridge patterns which can be seen with the naked eye. This nanocomposite also enhanced special properties including higher quality images, less contrast and easy visualization of LFP ridge patterns under daylight, as shown in Fig. 9(b, d).

3.4.11. LFP detection mechanism with reusable Pb^{2+}-CDs/Al_2O_3NFs nanocomposite

Scheme 5 illustrates the mechanism of process for LFP, where donor fingers were cleaned before any further work LFP detection was conducted by using the powder dusting method with reusable of Pb^{2+}-CDs/Al_2O_3NFs nanocomposite adsorbent as fingerprint powder. The fingerprint residue has some kind of oil components of amino acid, proteins and peptide. This reusable Pb^{2+}-CDs/Al_2O_3NFs nanocomposite was spread on the fingerprint residue and it was strongly coordinated with oil components to form complex and this resulted in clear fingerprint images and ridges. The extra reusable Pb^{2+}-CDs/Al_2O_3NFs nanocomposite adsorbent was removed by a squirrel brush. A clear fingerprint ridge was obtained due to the electrostatic interaction between the Pb^{2+}-CDs/Al_2O_3NFs nanocomposite adsorbent and oil components of the fingerprint residue. LFP images were captured by smart phone.

4. Conclusion

CDs/Al_2O_3NFs nanocomposite was used as an efficient adsorbent for fast and better removal of Pb^{2+} ions from the water samples. The adsorption behavior was determined by using Langmuir and Freundlich isotherm models. The maximum adsorption capacity was

suitable for Freundlich isotherm model and it was evaluated as 177.83 mg g^{-1} at 303 K. This adsorption process was better fitted with the pseudo-second order kinetic model than pseudo-first order. The thermodynamic parameters of ΔG_o and ΔH_o parameters showed spontaneous as well as exothermic adsorption processes. A reusable study was also carried out for LFP detection with Pb^{2+}-CDs/Al_2O_3NFs nanocomposite using a powder dusting method under normal light. This reusable nanocomposite was applied on various substrates to develop fingerprints. This reusable adsorbent has shown good potential as a labeling agent for LFP detection in forensic studies. Hence, once this adsorbent has reached its maximum lead loading it can be commercialized and sold to law enforcement officials for LFP detection instead of being discarded into the environment as secondary waste.

Declaration of Competing Interest

The authors declare that they have no known competing financial interests or personal relationships that could have appeared to influence the work reported in this paper.

Appendix A. Supplementary material

Supplementary data to this article can be found online at https://doi.org/10.1016/j.arabjc.2020.06.030.

References

Al Naggar, Y. et al, 2018. Environmental pollution by heavy metals in the aquatic ecosystems of Egypt. Open. Acc. J. Toxicol. 3,. https://doi.org/10.19080/OAJT.2018.03.555603 555603.

Alam, A.M., Park, B.Y., Ghouri, Z.K., Park, M., Kim, H.Y., 2015. Synthesis of carbon quantum dots from cabbage with down-and up-conversion photoluminescence properties: excellent imaging agent for biomedical applications. Green Chem. 17, 3791–3797. https://doi.org/10.1039/C5GC00686D.

Alberti, G., Amendola, V., Pesavento, M., Biesuz, R., 2012. Beyond the synthesis of novel solid phases: Review on modeling of sorption phenomena. Coord. Chem. Rev. 256, 28–45. https://doi.org/10.1016/j.ccr.2011.08.022.

Ali, I., Gupta, V.K., 2006. Advances in water treatment by adsorption technology. Nat. Protoc. 1, 2661–2667. https://doi.org/10.1038/nprot.2006.370.

Bala, T., Armstrong, G., Laffir, F., Thornton, R., 2011. Titania–silver and alumina–silver composite nanoparticles: Novel, versatile synthesis, reaction mechanism and potential antimicrobial application. J. Colloid Interface Sci. 356, 395–403. https://doi.org/10.1016/j.jcis.2011.01.044.

Barka, N., Abdennouri, M., El Makhfouk, M., Qourzal, S., 2013. Biosorption characteristics of cadmium and lead onto ecofriendly dried cactus (Opuntia ficus indica) cladodes. J. Environ. Chem. Eng. 1, 144–149. https://doi.org/10.1016/j.jece.2013.04.008.

Basavaraj, R.B., Nagabhushana, H., Darshan, G.P., Daruka Prasad, B., Rahul, M., Sharma, S.C., Sudaramani, R., Archana, K.V.,

2017. Red and green emitting CTAB assisted CdSiO3:Tb3 + /Eu3 + nanopowders as fluorescent labeling agents used in forensic and display applications. Dye. Pigm. 147, 364–377. https://doi.org/10.1016/j.dyepig.2017.08.011.

Bee, A., Talbot, D., Abramson, S., Dupuis, V., 2011. Magnetic alginate beads for Pb(II) ions removal from wastewater. J. Colloid Interface Sci. 362, 486–492. https://doi.org/10.1016/j.jcis.2011.06.036.

Bertoia, M.L., Mukamal, K.J., Cahill, L.E., Hou, T., Ludwig, D.S., Mozaffarian, D., Willett, W.C., Hu, F.B., Rimm, E.B., 2015. PLoS Med. 12,. https://doi.org/10.1371/journal.pmed.1001878 e1001878.

Bourlinos, A.B., Trivizas, G., Karakassides, M.A., Baikousi, M., Kouloumpis, A., Gournis, D., Bakandritsos, A., Hola, K., Kozak, O., Zboril, R., Papagiannouli, I., 2015. Green and simple route toward boron doped carbon dots with significantly enhanced nonlinear optical properties. Carbon 83, 173–179. https://doi.org/10.1016/j.carbon.2014.11.032.

Cai, W., Hu, Y., Yu, J., Wang, W., Zhou, J., Jaroniec, M., 2015. Template-free synthesis of hierarchical γ-Al$_2$O$_3$ nanostructures and their adsorption affinity toward phenol and CO$_2$. RSC Adv. 5, 7066–7073. https://doi.org/10.1039/C4RA11329B.

Cao, C.Y., Qu, J., Yan, W.S., Zhu, J.F., Wu, Z.Y., Song, W.G., 2012. Low-cost synthesis of flower like α-Fe$_2$O$_3$ nanostructures for heavy metal ion removal: adsorption property and mechanism. Langmuir 28, 4573–4579. https://doi.org/10.1021/la300097y.

Cantu, A.A., 2001. Silver Physical Developers for the Visualization of Latent Prints on Paper.

Chen, Y.H., Kuo, S.Y., Tsai, W.K., Ke, C.S., Liao, C.H., Chen, C.P., Wang, Y.T., Chen, H.W., Chan, Y.H., 2016. Dual colorimetric and fluorescent imaging of latent fingerprints on both porous and nonporous surfaces with near-infrared fluorescent semiconducting polymer dots. Anal. Chem. 88, 11616–11623. https://doi.org/10.1021/acs.analchem.6b03178.

Corr, S.A., 2012. Metal oxide nanoparticles. Nanosci. 31, 180–207. https://doi.org/10.1039/9781849734844-00180.

Cruz, A.A., Freire, R.M., Carneiro, S.V., Ferreira, O.P., Fechine, P.B., 2017. Carbon Quantum Dots: A Safe Tool to Learn about Quantum Phenomenon in Nanomaterials. J. Lab. Chem. Educ. 5, 48–54. https://doi.org/10.5923/j.jlce.20170503.02.

Champod, C., Lennard, C.J., Margot, P., Stoilovic, M., 2016. Fingerprints and Other Ridge Skin Impressions. CRC Press.

Chigondo, M., Paumo, H.K., Bhaumik, M., Pillay, K., Maity, A., 2018. Rapid high adsorption performance of hydrous cerium-magnesium oxides for removal of fluoride from water. J. Mol. Liq. 265, 496–509. https://doi.org/10.1016/j.molliq.2018.06.015.

Das, L., Kolar, P., Osborne, J.A., Classen, J.J., 2012. Adsorption of p-cresol on granular activated carbon. Agric. Eng. Int. 14, 37–49 http://www.cigrjournal.org/index.php/Ejounral/article/view/2171/1662.

Das, A., Shama, V., 2016. Synthesis and characterization of Eu3 + doped α-Al2O3 nanocrystalline powder for novel application in latent fingerprint development. Adv. Mater. Lett. 7, 302–306. https://doi.org/10.5185/amlett.2016.6310.

Den Besten, G., van Eunen, K., Groen, A.K., Venema, K., Reijngoud, D.J., Bakker, B.M., 2013. The role of short-chain fatty acids in the interplay between diet, gut microbiota, and host energy metabolism. J. Lipid Res. 54, 2325–2340. https://doi.org/10.1194/jlr.R036012.

Farooq, U., Kozinski, J.A., Khan, M.A., Athar, M., 2010. Biosorption of heavy metal ions using wheat based biosorbents–a review of the recent literature. Bioresource Technol. 101, 5043–5053. https://doi.org/10.1016/j.biortech.2010.02.030.

Fernandes, D., Krysmann, M.J., Kelarakis, A., 2015. Carbon dot based nanopowders and their application for fingerprint recovery. Chem. Comm. 51, 4902–4905. https://doi.org/10.1039/C5CC00468C.

Fifi, U., Winiarski, T., Emmanuel, E., 2013. Assessing the mobility of lead, copper and cadmium in a calcareous soil of Port-au-Prince, Haiti. Int. J. Environ. Res. Public Health 10, 5830–5843. https://doi.org/10.3390/ijerph10115830.

Gautam, P.K., Gautam, R.K., Banerjee, S., Chattopadhyaya, M.C., Pandey, J.D., 2016. Heavy metals in the environment: fate, transport, toxicity and remediation technologies. Nova. Sci. Publishers. 60, 101–130. ISBN: 978-1-63484-740-7.

Giles, C.H., Smith, D., Huitson, A., 1974. A general treatment and classification of the solute adsorption isotherm. I. Theoretical. J. Colloid Interface Sci. 47, 755–765. https://doi.org/10.1016/0021-9797(74)90252-5.

Guerra, D.L., Airoldi, C., DeSousa, K.S., 2008. Adsorption and thermodynamic studies of Cu(II) and Zn(II) on organofunctional-ized-kaolinite. Appl. Surf. Sci. 254, 5157–5163. https://doi.org/10.1016/j.apsusc.2008.02.017.

Gunatilake, S.K., 2015. Methods of Removing Heavy Metals from Industrial Wastewater. J. Multidiscip. Eng. Sci. Stud. 1, 1–18. ISSN: 2912-1309.

Hsieh, S.H., Horng, J.J., 2007. Adsorption behavior of heavy metal ions by carbon nanotubes grown on microsized Al$_2$O$_3$ particles. J. Univ. Sci. Technol. Beijing 14, 77–84. https://doi.org/10.1016/S1005-8850(07)60016-4.

Hua, M., Zhang, S., Pan, B., Zhang, W., Lv, L., Zhang, Q., 2012. Heavy metal removal from water/wastewater by nanosized metal oxides: a review. J. Hazard. Mater. 211–212, 317–331. https://doi.org/10.1016/j.jhazmat.2011.10.016.

Hutson, N.D., Yang, R.T., 1997. Theoretical basis for the Dubinin-Radushkevitch (DR) adsorption isotherm equation 3, 189–195. https://doi.org/10.1007/BF01650130.

Iqbal, N., Mobin, M., Rafiquee, M.Z., Al-Lohedan, H.A., 2013. Removal of Cu^{2+}, Cd^{2+}, Pb^{2+} and Hg^{2+} ions by the synthesized sodium dodecyl benzene sulphonate-based tin (IV) phosphate (SDBS-SnP) cation exchanger. Desalin. Water Treat. 51, 6688–6697. https://doi.org/10.1080/19443994.2013.765809.

Iqbal, M., Saeed, A., Zafar, S.I., 2009. FTIR spectrophotometry, kinetics and adsorption isotherms modeling, ion exchange, and EDX analysis for understanding the mechanism of Cd^{2+} and Pb^{2+} removal by mango peel waste. J. Hazard. Mater. 164, 161–171.

Jaishankar, M., Tseten, T., Anbalagan, N., Mathew, B.B., Beere-gowda, K.N., 2014. Toxicity, mechanism and health effects of some heavy metals. Interdiscip. Toxicol. 7, 60–72. https://doi.org/10.2478/intox-2014-0009.

Kang-Chung Ng, K., 2015. Hong Kong lawmaker Helena Wong moves from blunders to tainted water scandal. South China Morning Post (accessed on 26 July 2019).

Kim, Y.J., Jung, H.S., Lim, J., Ryu, S.J., Lee, J.K., 2016. Rapid Imaging of Latent Fingerprints Using Biocompatible Fluorescent Silica Nanoparticles. Langmuir 32, 8077–8083. https://doi.org/10.1021/acs.langmuir.6b01977.

Kosa, A., Al-Zhrani, G., Salam, M.S., 2012. Removal of heavy metals from aqueous solutions by multi-walled carbon nanotubes modified with 8-hydroxyquinoline. Chem. Eng. J. 181–182, 159–168. https://doi.org/10.1016/j.cej.2011.11.044.

Lasheen, M.R., El-Sherif, I.Y., Sabry, D.Y., El-Wakeel, S.T., El-Shahat, M.F., 2015. Removal of heavy metals from aqueous solution by multiwalled carbon nanotubes: equilibrium, isotherms, and kinetics. Desalin. Water Treat. 53, 3521–3530. https://doi.org/10.1080/19443994.2013.873880.

Lenntech, 2019. Lead and water: reaction mechanisms, environmental impact and health effects. https://www.lenntech.com/periodic/water/lead/lead-and-water.htm (accessed on 12/07/201).

Lee, S.J., Park, J.H., Ahn, Y.T., Chung, J.W., 2015. Comparison of heavy metal adsorption by peat moss and peat moss-derived biochar produced under different carbonization conditions. Water Air Soil Pollut. 226, 9. https://doi.org/10.1007/s11270-014-2275-4.

Li, H., Guo, X., Liu, J., Li, F., 2016a. A synthesis of fluorescent starch based on carbon nanoparticles for fingerprints detection. Opt. Mater. (Amst) 60, 404–410. https://doi.org/10.1016/j.optmat.2016.08.010.

Li, S., Zhang, G., Zhang, W., Zheng, H., Zhu, W., Sun, N., Zheng, Y., Wang, P., 2017. Microwave enhanced Fenton-like process for degradation of perfluorooctanoic acid (PFOA) using Pb-BiFeO$_3$/rGO as heterogeneous catalyst. Chem. Eng. J. 326, 756–764. https://doi.org/10.1016/j.cej.2017.06.037.

Li, W., Qiu, Y., Zhang, L., Jiang, L., Zhou, Z., Chen, H., Zhou, J., 2016b. Aluminum nanopyramid array with tunable ultraviolet–visible–infrared wavelength plasmon resonances for rapid detection of carbohydrate antigen 199. Biosens. Bioelectron. 79, 500–507. https://doi.org/10.1016/j.bios.2015.12.038.

Liu, J.H., Cao, L., LeCroy, G.E., Wang, P., Meziani, M.J., Dong, Y., Liu, Y., Luo, P.G., Sun, Y.P., 2015. Carbon "Quantum" Dots for Fluorescence Labeling of Cells. ACS Appl Mater Inter. 7, 19439–19445. https://doi.org/10.1021/acsami.5b05665.

Liu, W., Wang, T., Borthwick, A.G., Wang, Y., Yin, X., Li, X., Ni, J., 2013. Adsorption of Pb^{2+}, Cd^{2+}, Cu^{2+} and Cr^{3+} onto titanate nanotubes: competition and effect of inorganic ions. Sci. Total Environ. 456, 171–180. https://doi.org/10.1016/j.scitotenv.2013.03.082.

Lu, W., Qin, X., Liu, S., Chang, G., Zhang, Y., Luo, Y., Asiri, A.M., Al-Youbi, A.O., Sun, X., 2012. Economical, Green Synthesis of Fluorescent Carbon Nanoparticles and Their Use as Probes for Sensitive and Selective Detection of Mercury(II) Ions. Anal. Chem. 84, 5351–5357. https://doi.org/10.1021/ac3007939.

Luisa Cervera, M., Carmen Arnal, M., de la Guardia, M., 2003. Removal of heavy metals by using adsorption on alumina or chitosan. Anal. Bioanal. Chem. 375, 820–825. https://doi.org/10.1007/s00216-003-1796-2.

Madrakian, T., Afkhami, A., Ahmadi, M., 2013a. Adsorption and kinetic studies of seven different organic dyes onto magnetite nanoparticles loaded tea waste and removal of them from wastewater samples. Spectrochim. Acta Part A Mol. Biomol. Spectrosc. 99, 102–109. https://doi.org/10.1016/j.saa.2012.09.025.

Madrakian, T., Afkhami, A., Ahmadi, M., 2013b. Simple in situ functionalizing magnetite nanoparticles by reactive blue-19 and their application to the effective removal of Pb^{2+} ions from water samples. Chemosphere 90, 542–547. https://doi.org/10.1016/j.chemosphere.2012.08.025.

Meepho, M., Sirimongkol, W., Ayawanna, J., 2018. Samaria-doped Ceria Nanopowders for Heavy Metal Removal from Aqueous Solution. Mater. Chem. Phys. 214, 56–65. https://doi.org/10.1016/j.matchemphys.2018.04.083.

Mahdavi, S., Jalali, M., Afkhami, A., 2012. Removal of heavy metals from aqueous solutions using Fe3O4, ZnO, and CuO nanoparticles. J. Nanopart. Res. 14, 846. https://doi.org/10.1007/s11051-012-0846-0.

Mahdavi, S., Jalali, M., Afkhami, A., 2013. Heavy metals removal from aqueous solutions using TiO$_2$, MgO, and Al$_2$O$_3$ nanoparticles. Chem. Eng. Commun. 200, 448–470. https://doi.org/10.1080/00986445.2012.686939.

Mahdavi, S., Jalali, M., Afkhami, A., 2015. Heavy metals removal from aqueous solutions by Al$_2$O$_3$ nanoparticles modified with natural and chemical modifiers. Clean. Techn. Environ. Policy 17, 85–102. https://doi.org/10.1007/s10098-014-0764-1.

Mdoe, J.E., 2014. Agricultural Waste as Raw Materials for the Production of Activated Carbon: Can Tanzania Venture into this Business?. Huria: J. Open Univ. Tanzania. 16, 89–103. eISSN: 0856–6739.

Moret, S., Bécue, A., Champod, C., 2016. Functionalised silicon oxide nanoparticles for fingermark detection. Forensic Sci. Int. 259, 10–18. https://doi.org/10.1016/j.forsciint.2015.11.015.

Mukherjee, A., Mohammed Sadiq, I., Prathna, T.C., Chandrasekaran, N., 2011. Antimicrobial activity of aluminium oxide nanoparticles for potential clinical applications. Science against microbial pathogens: communicating current research and technological advances 1, 245–251.

Mubarak, N.M., Sahu, J.N., Abdullah, E.C., Jayakumar, N.S., 2016. Rapid adsorption of toxic Pb (II) ions from aqueous solution using multiwall carbon nanotubes synthesized by microwave chemical vapor deposition technique. J. Environ. Sci. 45, 143–155. https://doi.org/10.1016/j.jes.2015.12.025.

Nagashanmugam, K.B., Srinivasan, K., 2010. Evaluation of carbon derived fror Gingelly oil cake for the removal of lead(II) from aqueous solutions. J. Environ. Sci. Eng. 52, 349–360.

Niu, P., Liu, B., Li, Y., Wang, Q., Dong, A., Hou, H., Zhang, L., Gao, Y., Zhang, J., 2015. CdTe@SiO2/Ag nanocomposites as antibacterial fluorescent markers for enhanced latent fingerprint detection. Dye. Pigment. 119, 1–11. https://doi.org/10.1016/j.dyepig.2015.03.018.

Ntuli, V., Hapazari, I., 2012. Sustainable waste management by production of activated carbon from agroforestry residues. S. Afr. J. Sci. 109, 1–6. https://doi.org/10.1590/sajs.2013/1077.

Omorogie, M.O., Babalola, J.O., Unuabonah, E.I., 2016. Regeneration strategies for spent solid matrices used in adsorption of organic pollutants from surface water: a critical review. Desalin. Water Treat. 57, 518–544. https://doi.org/10.1080/19443994.2014.967726.

Peng, Y.K., Ye, L., Qu, J., Zhang, L., Fu, Y., Teixeira, I.F., McPherson, I.J., He, H., Tsang, S.C., 2016a. Trimethylphosphine-Assisted Surface Fingerprinting of Metal Oxide Nanoparticle by (31) P Solid-State NMR: A Zinc Oxide Case Study. J. Am. Chem. Soc. 138, 2225–2234. https://doi.org/10.1021/jacs.5b12080.

Peng, Y., Si, W., Li, X., Chen, J., Li, J., Crittenden, J., Hao, J., 2016b. Investigation of the Poisoning Mechanism of Lead on the CeO$_2$-WO$_3$ Catalyst for the NH–SCR Reaction via in Situ IR and Raman Spectroscopy Measurement. Environ. Sci. Technol. 50, 9576–9582. https://doi.org/10.1021/acs.est.6b02307-.

Prabakaran, E., Pillay, K., 2020. Synthesis and characterization of fluorescent N-CDs/ZnONPs nanocomposite for latent fingerprint detection by using powder brushing method. Arab. J. Chem. 13, 3817–3835. https://doi.org/10.1016/j.arabjc.2019.01.004.

Qin, G., Zhang, M.Q., Zhang, Y., Zhu, Y., Liu, S.L., Wu, W.J., Zhang, X.J., 2013. Visualizing latent fingerprints by electrodeposition of metal nanoparticles. J. Electroanal. Chem. 693, 122–126. https://doi.org/10.1016/j.jelechem.2013.01.016.

Qin, D., Hu, X., Dong, Y., Mamat, X., Li, Y., Wågberg, T., Hu, G., 2018. An Electrochemical Sensor Based on Green γ-AlOOH-Carbonated Bacterial Cellulose Hybrids for Simultaneous Determination Trace Levels of Cd(II) and Pb(II) in DrinkingWaterJ. Electrochem. Soc. 165, B328–B334. https://doi.org/10.1149/2.1321807jes.

Reddy, D.H., Lee, S.M., Seshaiah, K., 2012. Removal of Cd(II) and Cu(II) from Aqueous Solution by Agro Biomass: Equilibrium, Kinetic and Thermodynamic Studies. Environ. Eng. Res. 17, 125–132. https://doi.org/10.4491/eer.2012.17.3.125.

Rohini, B.S., Nagabhushana, H., Darshan, G.P., Basavaraj, R.B., Sharma, S.C., Sudarmani, R., 2017. Fabricated CeO$_2$ nanopowders as a novel sensing platform for advanced forensic, electrochemical and photocatalytic applications. Appl. Nanosci. 7, 815–833. https://doi.org/10.1007/s13204-017-0611-x.

Saad, A.H.A., Azzam, A.M., El-Wakeel, S.T., Mostafa, B.B., Abd El-latif, M.B., 2018. Removal of toxic metal ions from wastewater using ZnO@Chitosan coreshell Nanocomposite. Environ. Nanotechnol. Monit. Manage. 9, 67–75. https://doi.org/10.1016/j.enmm.2017.12.004.

Sadeghi Pouya, E., Abolghasemi, H., Esmaieli, M., Fatoorehchi, H., Hashemi, S.J., Salehpour, A., 2015. Batch adsorptive removal of benzoic acid from aqueous solution onto modifi ed natural vermiculite: Kinetic, isotherm and thermodynamic studies. J. Ind. Eng. Chem. 31, 199–215. https://doi.org/10.1016/j.jiec.2015.06.024.

Sagar, N.A., Pareek, S., Sharma, S., Yahia, E.M., Lobo, M.G., 2018. Fruit and Vegetable Waste: Bioactive Compounds, Their Extraction, and Possible Utilization. Compr. Rev. Food Sci. Food Saf. 17, 512–531. https://doi.org/10.1111/1541-4337.12330.

Salam, M.A., Makki, M.S.I., Abdelaal, M.Y.A., 2011. Preparation and characterization of multi-walled carbon nanotubes/chitosan nanocomposite and its application for the removal of heavy metals

from aqueous solution. J. Alloy. Compd. 509, 2582–2587. https://doi.org/10.1016/j.jallcom.2010.11.094.

Santos Yabe, M.J., de Oliveira, E., 2003. Heavy metals removal in industrial effluents by sequential adsorbent treatment. Adv. Environ. Res. 7, 263–272. https://doi.org/10.1016/S1093-0191(01)00128-9.

Saruchi, Kumar V., 2019. Adsorption kinetics and isotherms for the removal of rhodamine B dye and Pb^{+2} ions from aqueous solutions by a hybrid ion-exchanger. Arabian J. Chem. 12, 316–329. https://doi.org/10.1016/j.arabjc.2016.11.009.

Sen, T.K., Mohammod, M., Maitra, S., Dutta, B.K., 2010. Removal of cadmium from aqueous solution using castor seed hull: A kinetic and equilibrium study. Clean-Soil, Air, Water 38, 850–858. https://doi.org/10.1002/clen.200900246.

Shajahan, S., Arumugam, P., Rajendran, R., Munusamy, A.P., 2020. Optimization and detailed stability study on Pb doped ceria nanocubes for enhanced photodegradation of several anionic and cationic organic pollutants. Arabian J. Chem. 13, 1309–1322. https://doi.org/10.1016/j.arabjc.2017.11.001.

Sharma, Y.C., Srivastava, V., Mukherjee, A.K., 2010. Synthesis and Application of Nano-Al₂O₃ Powder for the Reclamation of Hexavalent Chromium from Aqueous Solutions. J. Chem. Eng. Data 55, 2390–2398. https://doi.org/10.1021/je900822j.

Shi, X., Wei, W., Fu, Z., Gao, W., Zhang, C., Zhao, Q., Deng, F., Lu, X., 2019. Review on Carbon Dots in Food Safety Applications. Talanta 194, 809–821. https://doi.org/10.1016/j.talanta.2018.11.005.

Sodhi, G.S., Kaur, J., 2016. Physical developer method for detection of latent fingerprints: a review. Egy. J. Forensic. Sci. 6, 44–47. https://doi.org/10.1016/j.ejfs.2015.05.001.

Song, W., Mao, Z., Liu, X., Lu, Y., Li, Z., Zhao, B., Lu, L., 2012. Detection of protein deposition within latent fingerprints by surface-enhanced Raman spectroscopy imaging. Nanoscale. 4, 2333–2338. https://doi.org/10.1039/C2NR12030E.

Srivastava, V., Weng, C.H., Singh, V.K., Sharma, Y.C., 2011. Adsorption of Nickel Ions from Aqueous Solutions by Nano Alumina: Kinetic, Mass Transfer, and Equilibrium Studies. J. Chem. Eng. Data 56, 1414–1422. https://doi.org/10.1021/je101152b.

Toledo, R.R., Santoyo, V.R., Sánchez, D.M., Rosales, M.M., 2018. Effect of aluminum precursor on physicochemical properties of Al2O3 by hydrolysis/precipitation method. Nova Scientia. 10, 83–99. https://doi.org/10.21640/ns.v10i20.1217.

Toth, 1971. State equations of the solid gas interface layer. Acta Chim. Hung. 69, 311–317.

Valdesueiro, D., Prabhu, M.K., Guerra-Nunez, C., Sandeep, C.S., Kinge, S., Siebbeles, L.D., de Smet, L.C., Meesters, G.M., Kreutzer, M.T., Houtepen, A.J., van Ommen, J.R., 2016. Deposition Mechanism of Aluminum Oxide on Quantum Dot Films at Atmospheric Pressure and Room Temperature. J. Phys. Chem. C 120, 4266–4275. https://doi.org/10.1021/acs.jpcc.5b11653.

Venkatesan, G., Senthilnathan, U., Rajam, S., 2014. Cadmium removal from aqueous solutions using hybrid eucalyptus wood based activated carbon: Adsorption batch studies. Clean Technol. Environ. Policy 16, 195–200. https://doi.org/10.1007/s10098-013-0628-0.

Wang, S., Ariyanto, E., 2007. Competitive adsorption of malachite green and Pb ions on natural zeolite. J. Colloid Interface Sci. 314, 25–31. https://doi.org/10.1016/j.jcis.2007.05.032.

Wang, J., Li, Y., Lv, Z., Xie, Y., Shu, J.J., Alsaedi, A., Hayat, T., Chen, C., 2019. Exploration of the adsorption performance and mechanism of zeolitic imidazolate framework-8@graphene oxide for Pb(II) and 1-naphthylamine from aqueous solution. J. Colloid Interface 542, 410–420. https://doi.org/10.1016/j.jcis.2019.02.039.

Xu, Q., Pu, P., Zhao, J., Dong, C., Gao, C., Chen, Y., Chen, J., Liu, Y., Zhou, H., 2015. Preparation of highly photoluminescent sulfur-doped carbon dots for Fe(iii) detection. J. Mater. Chem. A 3, 542–546. https://doi.org/10.1039/C4TA05483K.

Yalamaç, E., Trapani, A., Akkurt, S., 2014. Sintering and microstructural investigation of gamma–alpha alumina powders. Eng. Sci. Technol. Int. J. 17, 2–7. https://doi.org/10.1016/j.jestch.2014.02.001.

Yang, S., Hu, J., Chen, C., Shao, D., Xiangke Wang, X., 2019. Correction to Mutual Effects of Pb(II) and Humic Acid Adsorption on Multiwalled Carbon Nanotubes/Polyacrylamide Composites from Aqueous Solutions. Environ. Sci. Technol. 53, 13546. https://doi.org/10.1021/acs.est.9b06367.

Zhang, T., Zhai, Y., Wang, H., Zhu, J., Xu, L., Dong, B., Song, H., 2016a. Facilely prepared carbon dots and rare earth ion doped hybrid composites for ratio-metric pH sensing and white-light emission. RSC Adv. 6, 61468–61472. https://doi.org/10.1039/C6RA11386A.

Zhang, L., Zhang, H., Yu, X., 2011. Investigation of solution chemistry effects on sorption behavior of Cu(II) on ZSM-5 zeolite. Water Environ. Res. 83, 2170–2177. https://doi.org/10.2175/106143011x12989211841250.

Zhang, R., Chen, W., 2014. Nitrogen-doped carbon quantum dots: Facile synthesis and application as a "turn-off" fluorescent probe for detection of Hg^{2+} ions. Biosens. Bioelectron. 55, 83–90. https://doi.org/10.1016/j.bios.2013.11.074.

Zhang, L., Wu, Y., Zhang, L., Wang, Y., Li, M., 2016b. Synthesis and characterization of mesoporous alumina with high specific area via co-precipitation method. Vacuum 133, 1–6. https://doi.org/10.1016/j.vacuum.2016.08.005.

Zhou, L.L., Li, C., Zhao, L.K., Zeng, G.G., Gao, L., Wang, Y., Yu, M., 2016. The poisoning effect of PbO on Mn-Ce/TiO₂ catalyst for selective catalytic reduction of NO with NH₃ at low temperature. Appl. Surf. Sci. 389, 532–539. https://doi.org/10.1016/j.apsusc.2016.07.136.

Zheng, H., Gao, Y., Zhu, K., Wang, Q., Wakeel, M., Wahid, A., Alharbi, N.S., Chen, C., 2018. Investigation of the adsorption mechanisms of Pb(II) and 1-naphthol by β-cyclodextrin modified graphene oxide nanosheets from aqueous solution. J. Colloid Interface Sci. 530, 154–162. https://doi.org/10.1016/j.jcis.2018.06.083.

Zhu, J., Lin, X., Wu, P., Zhou, Q., Luo, X., 2015. Fluoride removal from aqueous solution by Al (III)–Zr (IV) binary oxide adsorbent. Appl. Surf. Sci. 357, 91–100. https://doi.org/10.1016/j.apsusc.2015.09.012.

Zhu, H., Tan, X., Tan, L., Chen, C., N.S., Alharbi, Hayat, T., Fang, M., Wang, X., 2018. Biochar Derived from Sawdust Embedded with Molybdenum Disulfide for Highly Selective Removal of Pb2+. ACS Appl. Nano Mater. 1, 2689–2698. https://doi.org/10.1021/acsanm.8b00388.

Zwain, H.M., Vakili, M., Dahlan, I., 2014. Waste Material Adsorbents for Zinc Removal from Wastewater: A Comprehensive Review. Int. J. Chem. Eng. 2014, 1–13. https://doi.org/10.1155/2014/347912.